

Emissivity and reflection model for calculating unpolarized isotropic water surface-leaving radiance in the infrared. I: Theoretical development and calculations

Nicholas R. Nalli,^{1,*} Peter J. Minnett,² and Paul van Delst³

¹Perot Systems Government Services, Inc., National Oceanic and Atmospheric Administration, National Environmental Satellite, Data, and Information Service, Center for Satellite Applications and Research, 5211 Auth Road, Camp Springs, Maryland 20746, USA

²University of Miami, Rosenstiel School of Marine and Atmospheric Science, 4600 Rickenbacker Causeway, Miami, Florida 33149, USA

³University of Wisconsin, Cooperative Institute for Meteorological Satellite Studies, W/NP2, 5200 Auth Road, Camp Springs, Maryland 20746, USA

*Corresponding author: Nick.Nalli@noaa.gov

Received 28 November 2007; revised 23 April 2008; accepted 26 May 2008;
posted 2 June 2008 (Doc. ID 90171); published 11 July 2008

Although published sea surface infrared (IR) emissivity models have gained widespread acceptance for remote sensing applications, discrepancies have been identified against field observations obtained from IR Fourier transform spectrometers at view angles $\gtrsim 40^\circ$. We therefore propose, in this two-part paper, an alternative approach for calculating surface-leaving IR radiance that treats both emissivity and atmospheric reflection in a systematic yet practical manner. This first part presents the theoretical basis, development, and computations of the proposed model. © 2008 Optical Society of America

OCIS codes: 010.0280, 010.5620, 280.4991, 280.6780.

1. Introduction

The infrared (IR) spectral emissivity of the earth's surface is a critical component of environmental satellite remote sensing applications requiring accurate radiative transfer modeling. This is particularly true in hyperspectral microwindows (i.e., spectral regions with high atmospheric transmittance found between absorption lines), where a mere 0.5% departure in emissivity can result in significant perturbations ($\approx 0.3\text{--}0.4\text{ K}$) in apparent brightness temperatures. Accurate remote sensing of the oceans is especially critical given their high thermal inertia and geographic extent.

For these reasons there has been much work devoted to the modeling of the IR spectral emissivity of wind-roughened water surfaces [1–13]. Most published models explicitly calculate emissivity spectra for a given set of optical constants, emission zenith angles, and local wind speeds. Using the Cox and Munk [14,15] isotropic probability density function (PDF), Masuda *et al.* [1] first published, and conveniently tabulated, their facet model calculations almost two decades ago, although their results were not widely used initially. Yoshimori *et al.* [2,3], apparently unaware of the earlier work by Masuda *et al.* [1] and (surprisingly) Cox and Munk [14,15], independently developed a facet model based upon a wave spectral model with the latter paper being the first to utilize anisotropic wave slope statistics [3]. Later, Watts *et al.* [4] and Wu and Smith [5] explicitly expanded upon

the Masuda *et al.* [1] model by including additional physics (viz., reflected emissions), with the latter of which showing improved agreement with a limited set of field observations [16] over Masuda *et al.* Around the same time, Freund *et al.* [6] developed their model using the anisotropic Cox–Munk [14,15] wave slope statistics. Shaw and Marston [7] were the first to provide simple calculations of polarized emissivity, followed by Henderson *et al.* [9] who rigorously achieved this along with multiple reflections and shadowing using a Monte Carlo model. Meanwhile, Nalli *et al.* [8] argued the importance of accounting for reflected downwelling atmospheric radiance in a consistent manner, then proceeded to derive a simplified quasi-specular [17] reflectance model physically consistent with the Wu and Smith [5] emissivity model. More recently, within the past couple years, a number of improved unpolarized analytical models have been proposed. Masuda [12] revised his model to account for reflected emissions (in a similar but more physically consistent manner than either Watts *et al.* or Wu and Smith), and a series of interrelated papers describing analytical models of increasing sophistication were also published [10,11,13]. Bourlier [10] derived the first model to utilize the full non-Gaussian, anisotropic Cox–Munk wave slope statistics. A year later, Bourlier [11] derived the first analytical model to take rigorously into account multiple reflections of surface emissions (for Gaussian statistics). Finally, Caillault *et al.* [13], using a published wave spectrum, were the first to take into account surface wave slope variability as a function of the spatial scale (footprint) and emission angle, with the realism of their model dramatically illustrated through graphics of simulated sun glitter.

A number of these models [1,4,5] have now gained widespread acceptance within the satellite remote sensing community. For example, the Wu–Smith model [5] is currently used within the U.S. National Oceanic and Atmospheric Administration, National Centers for Environmental Prediction Global Data Assimilation System [18], as well as by the U.S. National Aeronautics and Space Administration, the Atmospheric Infrared Sounder (AIRS) Science Team [19], and radiative transfer models (RTMs).

In spite of the aforementioned progress and maturity in emissivity modeling, field observations obtained at sea over the past decade from the Marine Atmospheric Emitted Radiance Interferometer (M-AERI) [16,20], a high-accuracy sea-going IR Fourier transform spectrometer (FTS), have revealed discrepancies between calculation and observation at larger observing angles and wind speeds [8,21]. Specifically, emissivity spectra obtained by Hanafin and Minnett [21] suggest an underestimation of modeled emissivity at observing angles $\gtrsim 55^\circ$. They found the magnitude of the discrepancy to be significant in IR window regions, especially in the longwave IR (LWIR) (up to 0.4 K in equivalent brightness temperature). Their data show an unexpected increase of emissivity with wind speed,

whereas, with the exception of Watts *et al.* (cf. Figs. 11 and 12 of Ref. [4]), none of the aforementioned models predict such an increase. The Watts model predicted an increase in surface brightness temperatures with wind speed when reflected downwelling was properly taken into account, and M-AERI spectra observed by Nalli *et al.* [8] corroborated an underestimation in modeled surface brightness when the reflectance was not properly taken into account.

Thus, given the accuracy requirements for environmental satellite parameters (e.g., sea surface temperatures) along with the radiometric accuracy and microwindow selection of current state-of-the-art satellite IR spectrometers (AIRS and the European Organisation for the Exploitation of Meteorological Satellites Infrared Atmospheric Sounding Interferometer), it behooves us to ascertain the cause of the discrepancy and, if possible, propose a practical solution. In this the first (Part I) of two papers, we begin by emphasizing that the ultimate practical goal of modeling IR emissivity is, in fact, to model the surface-leaving radiance (SLR). Based on the working hypothesis that the apparent observed bias of standard models originates from their treating only the emitted component of SLR (i.e., the emissivity), while not providing a self-consistent approximation for the reflected component [4,8] (as elaborated in Subsection 2.B.2), we thus propose to derive a systematic and practical method for calculating wind-roughened water SLR. From our standpoint it is equally important that the derived model does not introduce a significant computational burden within operational processing systems. Given the difficulty in modeling quasi-specular reflected downwelling, it is this last consideration that poses the greatest challenge in this endeavor, which is the subject of the present paper. In our companion paper (Part II), the model is shown to have improved agreement with observations over the standard models using an exhaustive set of hyperspectral FTS field measurements acquired at sea.

2. Theoretical Development

Assuming a plane-parallel atmosphere with azimuthal symmetry, the IR radiative transfer equation (RTE) for the field of view (FOV) of a downlooking sensor positioned near the surface, observing at local zenith emission angle θ_0 and quasi-monochromatic wavenumber ν , is given by

$$R_{\nu s}(\theta_0) = \epsilon_\nu(\theta_0)B_\nu(T_s) + 2 \int_0^{\frac{\pi}{2}} r_\nu(\theta, \theta_0)I_{\nu a}^\downarrow(\theta) \cos(\theta) \sin(\theta) d\theta, \quad (1)$$

where $R_{\nu s}(\theta_0)$ is the SLR (in $\text{mW m}^{-2} \text{sr}^{-1} \text{cm}$), $\epsilon_\nu(\theta_0)$ is the effective FOV surface emissivity, B_ν is the Planck blackbody function, T_s is the surface skin temperature, θ is the local zenith incidence angle of downwelling rays, $r_\nu(\theta, \theta_0)$ is the bidirectional

reflectance, $I_{\nu a}^{\downarrow}(\theta)$ is the downwelling atmospheric-emitted intensity (radiance), and the atmospheric path attenuation and emission between the observer and the surface are assumed to be negligible in spectral window regions. $I_{\nu a}^{\downarrow}(\theta)$ may be calculated as

$$I_{\nu a}^{\downarrow}(\theta) = \int_{T_{\nu s}}^1 B_{\nu}[T(p)]dT_{\nu}(p_s, p; \theta), \quad p_s > p, \quad (2)$$

where $T(p)$ is the atmospheric temperature at pressure level p , and the transmittance profile from the surface pressure p_s to p , $T_{\nu}(p_s, p; \theta)$, along with the total column transmittance, $T_{\nu s} \equiv T_{\nu}(p_s, 0; \theta)$, must be computed from a suitable uplooking transmittance model.

The complexity of the bidirectional reflectance integral in Eq. (1) coupled with the computational demands of accurately calculating $I_{\nu a}^{\downarrow}(\theta)$ from Eq. (2) for multiple θ renders the exact calculation of the surface reflectance a difficult task. Fortunately, however, this term is of second order, typically more than an order of magnitude less than the emission term, and thus approximations may be employed. Because ocean surface reflectance is quasi-specular (i.e., diffuse with a significant specular component, the reflection lobe having a strong peak on or about the specular angle) [8,17], it is common practice to treat the bidirectional reflectance as either Lambertian or specular. Based on the literature currently available, it is more common (and probably accurate) to assume specularity, in which case the bidirectional reflectance becomes a delta function. Equation (1) is then approximated simply as [4,16,20,22–30]

$$R_{\nu s}(\theta_0) \approx \epsilon_{\nu}(\theta_0)B_{\nu}(T_s) + r_{\nu}(\theta_0)I_{\nu a}^{\downarrow}(\theta_0), \quad (3)$$

where it is usually assumed that $r_{\nu}(\theta_0) \approx 1 - \epsilon_{\nu}(\theta_0)$ from conservation of energy. Equation (3) thus suggests that SLR may be determined given the FOV surface emissivity, $\epsilon_{\nu}(\theta_0)$, along with a single calculation (or measurement) of downwelling atmospheric radiance at the emission angle, θ_0 . Although Eq. (3) assumes rough surface specular reflection as an approximation (i.e., the second term on the right-hand side), published emissivity models [1–6,9–13] allow the higher magnitude emission term (i.e., the first term on the right-hand side) to be correctly treated as quasi-specular. The basis for calculating $\epsilon_{\nu}(\theta_0)$ is the geometrical wave-slope facet model described below.

A. Facet Model of Rough Water Surface Emissivity

In this subsection we provide a brief review of the facet model of a wind-roughened water surface as relevant to the present work. For details on the derivations, including diagrams, refer to Nalli *et al.* [8] and the references therein.

Assuming the surface curvature arising from wave slopes within the sensor FOV is small with respect to IR wavelengths [5,8], the scattered electromagnetic field from each point on the surface is equivalent to that specularly reflected from tangent planes at those points (i.e., the geometrical optics limit). Assuming thermodynamic equilibrium at the air-sea interface, conservation of energy requires that the emissivity at each wave facet is 1 minus the directional reflectivity

$$\epsilon(N_{\nu}, \Theta_i) = 1 - \rho(N_{\nu}, \Theta_i), \quad (4)$$

where N_{ν} is the complex index of refraction, Θ_i is the incidence angle measured with respect to the local normal, and ρ is the Fresnel reflectance coefficient. For sensors with little or no polarization sensitivity (e.g., M-AERI), the reflectance coefficient for radiance is given by

$$\rho(N_{\nu}, \Theta_i) = \frac{1}{2}[\rho_{\parallel}(N_{\nu}, \Theta_i)^2 + \rho_{\perp}(N_{\nu}, \Theta_i)^2], \quad (5)$$

where the polarized reflectances for intensities are obtained by taking the square of the absolute value of the amplitude coefficients, ρ_{\parallel} and ρ_{\perp} , which correspond to the E fields parallel and perpendicular to the plane of incidence, respectively. Given a statistical description of the distribution of wave slopes for facets visible (i.e., not shadowed) to the sensor FOV, the mean emissivity of the rough surface can, in principle, be defined exactly as the ensemble effect of all such facets [31].

Cox and Munk [14,15] first observed from aerial photographs that the wave-slope distribution may be modeled as approximately Gaussian with the variance, σ^2 , described by a linear function of surface wind speed, \bar{U} (see Appendix A). This provided the foundation for much of the subsequent development of facet models for IR emission from rough water surfaces [1,4–12]. A coordinate transformation can be applied to express slope components z_x and z_y conveniently in terms of the local zenith cosine and azimuth angle with the model emissivity assuming the basic form [1,4,5,7,8,12]

$$\bar{\epsilon}(N_{\nu}, \theta_0, \bar{U}) = \frac{2}{\mu_0} \int_0^1 \frac{p(\mu_n, \sigma^2)}{\mu_n^4} \int_0^{\pi} [1 - \rho(N_{\nu}, \Theta_i)] \cos(\Theta_i) d\varphi_n d\mu_n, \quad (6)$$

where φ_n is the azimuth angle of a facet normal vector (measured relative to the observer), μ_n is the cosine of the local zenith angle of a facet normal vector (θ_n), $\Theta_i = \Theta_i(\mu_0, \mu_n, \varphi_n)$ is the facet incidence angle, $\mu_0 = \cos(\theta_0)$ is the zenith emission angle, and

$p(\mu_n, \sigma^2)$ is the PDF for wave slopes with inclination μ_n and variance $\sigma^2(\bar{U})$. In using numerical quadrature to integrate Eq. (6), the lower limit of the facet normal angle μ_n integration is adjusted from 0 to $\mu_{n1}(\bar{U}) \geq 0$ for quadrature efficiency [5,8]. Although Eq. (6) is the basic facet model equation, additional physics are included to account for wave shadowing and reflected emissions from the surface as described below.

1. Wave Shadowing

All models referenced in this paper have accounted for wave shadowing using various schemes. From geometrical reasoning, self-shadowing of waves can be accounted for in an exact manner by excluding the backsides of facets from the integration. In this work, this is achieved simply by reducing the upper limit of the azimuth angle integration to $\varphi_{n2}(\theta_0, \theta_n) \leq \pi$ as follows [8]:

$$\varphi_{n2}(\theta_0, \theta_n) = \begin{cases} \pi, & -\cot \theta_0 \cot \theta_n \leq -1 \vee \theta_0 = 0^\circ \\ \arccos(-\cot \theta_0 \cot \theta_n), & -1 < -\cot \theta_0 \cot \theta_n \leq 1 \wedge \theta_0 > 0^\circ \\ 0, & -\cot \theta_0 \cot \theta_n > 1 \wedge \theta_0 > 0^\circ \end{cases} \quad (7)$$

Shadowing caused by other waves is more difficult to account properly for. While Bourlier [10] recently succeeded in applying a generalized anisotropic shadowing and illumination function in slope coordinates (i.e., without a coordinate transformation to facet normal angles), we follow the conventional approach of applying the well-established method of Saunders [32,33]. We note that there has been duplication and even some confusion in the past regarding this convention that warrants further clarification. Saunders [32,33] proposed a “slope-shadowing factor,” $S(\theta_0, z_x, z_y)$, whereby $S \rightarrow 1$ would imply no shadowing and $S \rightarrow 0$ would imply total shadowing. The form of S was derived by first assuming that all the remaining slopes (i.e., those facing the observer) are shadowed equally, therefore rendering it invariant within the adjusted limits of the remaining definite integral, $[0, \varphi_{n2}]$, leaving it a function of θ_0 and σ^2 only. Then, considering a hypothetical black surface [33],

$$B_\nu(T_s) = 2\mu_0^{-1}S(\theta_0, \sigma^2) \int_{\mu_{n1}}^1 \mu_n^{-4} p(\mu_n, \sigma^2) \int_0^{\varphi_{n2}} B_\nu(T_s) \times \cos(\Theta_i) d\varphi_n d\mu_n, \quad (8)$$

$$\Rightarrow S(\theta_0, \sigma^2) = \frac{1}{2\mu_0^{-1} \int_{\mu_{n1}}^1 \mu_n^{-4} p(\mu_n, \sigma^2) \int_0^{\varphi_{n2}} \cos(\Theta_i) d\varphi_n d\mu_n}, \quad (9)$$

given that $B_\nu(T_s)$ is constant. When written in this form, we see that the Saunders shadowing factor is simply a normalization factor, allowing one to derive a normalized wave-slope PDF [6,8,34,35] defined as

$$P(\mu_n, \mu_0, \Theta_i, \sigma^2) \equiv 2\mu_0^{-1} \mu_n^{-4} \cos(\Theta_i) p(\mu_n, \sigma^2) S(\theta_0, \sigma^2), \quad (10)$$

which ensures that $\int_{\mu_n} \int_{\varphi_n} P d\varphi_n d\mu_n = 1$ [6,8]. Masuda *et al.* [1], apparently unaware of Saunders’ earlier work, independently proposed an equivalent scheme from energy conservation reasoning. Later investigators [4–6,8,34,35] also employed this basic scheme. However, it was Wu and Smith [5] who first correctly

pointed out that their method, along with Masuda’s [1], was identical to Saunders’ (Masuda himself later acknowledged this [12]). Zeisse [34], Freund *et al.* [6], and Zeisse *et al.* [35], who apparently did not recognize the similarity of their methods to that of Saunders’, called Eq. (10) the “interaction probability density” (e.g., see Eqs. 4, 5, and 6 in Freund *et al.* [6]). Nalli *et al.* [8], aware of Wu and Smith’s observation but unaware of these three papers, simply called it a normalized PDF. We believe that much of this past confusion may have been due to the fact that Saunders himself never wrote Eq. (9) explicitly, but instead analytically evaluated the double integral in Eq. (8) (in slope coordinates, assuming Gaussian p) to obtain

$$S(\theta_0, \sigma^2) = 2[1 + \text{erf}(v) + (v\sqrt{\pi})^{-1} \exp(-v^2)]^{-1}, \quad (11)$$

where erf is the error function and $v = v(\theta_0, \sigma^2)$ is given by

$$v(\theta_0, \sigma^2) = \frac{\cot(\theta_0)}{\sqrt{2\sigma^2}}. \quad (12)$$

$$p_s(\theta) = 0$$

$$p_s(\theta) = 1$$

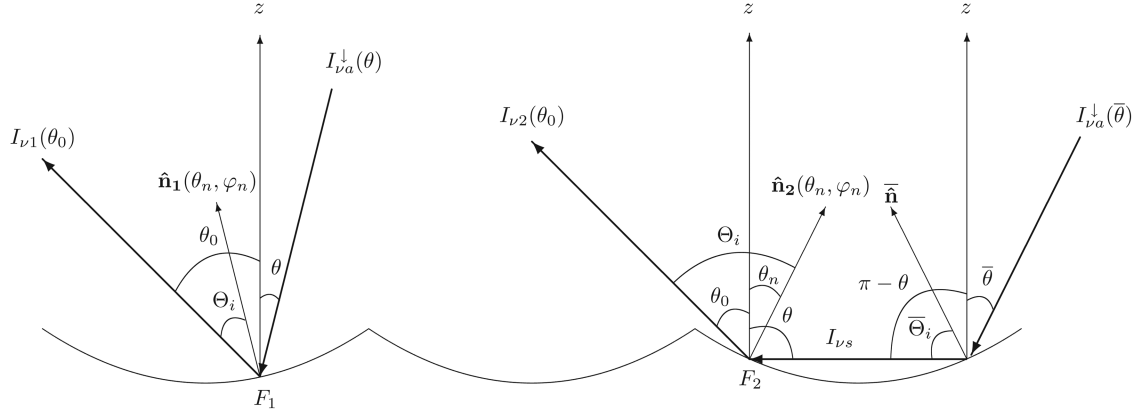


Fig. 1. Ray-trace schematic for modeling SLR from wave facets. The left wave facet, F_1 , shows incident rays originating from the sky ($p_s = 0$), whereas the right facet, F_2 , shows incident rays from the surface ($p_s = 1$) including SESR and SRSR contributions (note that for consistency with equations in the text, we use the same variables for F_1 and F_2 angles even though the magnitudes obviously differ). Here the radiance leaving F_1 would be given by $I_{\nu 1}(\theta_0) = [1 - \rho_{\nu}(\Theta_i)]B_{\nu}(T_s) + \rho_{\nu}(\Theta_i)I_{\nu a}^{\downarrow}(\theta)$ and the leaving F_2 would be $I_{\nu 2}(\theta_0) = [1 - \rho_{\nu}(\Theta_i)]B_{\nu}(T_s) + \rho_{\nu}(\Theta_i)I_{\nu s}$, where $I_{\nu s} \equiv [I_{\nu se}(\pi - \theta) + I_{\nu sr}(\pi - \theta)]$.

Because Saunders defined his shadowing factor in terms of Eqs. (11) and (12), its normalization form in Eq. (9) was not immediately obvious.

2. Reflected Emissions

Reflected surface emissions, which effectively enhance the mean emissivity, are accounted for by deriving a reduced Fresnel reflectivity

$$\begin{aligned} \rho^{-}(N_{\nu}, \Theta_i, \bar{U}) &\equiv \rho(N_{\nu}, \Theta_i) \\ &- \rho(N_{\nu}, \Theta_i)p_s(\theta)\bar{\epsilon}(N_{\nu}, \pi - \theta, \bar{U}), \end{aligned} \quad (13)$$

where $\bar{\epsilon}$ is first computed without reflected emissions, θ is the zenith incidence angle at the wave facet (see Fig. 1, right), and $p_s(\theta)$ is the probability of a ray originating from the surface (discussed in more detail in Subsection 2.B.2). This approach was first proposed by Watts *et al.* [4] and termed surface-emitted, surface-reflected (SESR) emission. Substituting into Eq. (6) P for p and ρ^{-} for ρ results in [4,5,8]

$$\begin{aligned} \bar{\epsilon}^{+}(N_{\nu}, \theta_0, \bar{U}) &= 1 - \int_{\mu_{n1}}^1 \int_0^{\varphi_{n2}} \rho^{-}(N_{\nu}, \Theta_i, \bar{U}) \\ &P(\mu_n, \mu_0, \Theta_i, \sigma^2) d\varphi_n d\mu_n. \end{aligned} \quad (14)$$

The two most used analytical emissivity models [4,5] are essentially based on Eq. (14). The primary approximations made in its derivation lie in the treatment of multiple reflections and wave shadowing. While there are no clear-cut estimates as to what the total errors introduced by these approximations

are, they are certainly of second order. Henderson *et al.* [9] addressed these problems in a more explicit manner using a Monte Carlo facet model, but the implementation of such a model is computationally burdensome. Both Henderson *et al.* [9] and Wu and Smith [36] have shown their calculations to agree reasonably well with a limited set emissivity measurements obtained using a modified AERI instrument[16].

B. Self-Consistent Models for Surface-Leaving Radiance

Given the modeled emissivity calculated from Eq. (14), the simple radiative transfer approximation in Eq. (3) is one of the more common and reasonably accurate ways of calculating the SLR as already indicated. The approximation in Eq. (3) consists in assuming the FOV bidirectional reflection to be specular, that is, lacking a component of diffuse incident radiation. However, because Eq. (14) is implicitly quasi-specular [17] (i.e., diffuse with a significant specular component), it is more accurate to treat the reflected atmospheric radiance in a consistent manner ideally without requiring an on-the-spot hemispheric integration of downwelling radiances. We develop two methods for achieving this below.

1. Ensemble-Mean Reflection Geometry

We may formulate a self-consistent specular model approximation to Eq. (1) by considering only specular reflections that arise from the ensemble-mean surface facet inclination [37]. The SLR is approximated as

$$R_{\nu s}(\theta_0) \approx B_{\nu}(T_s) - \rho_{\nu}(\bar{\Theta}_i)[B_{\nu}(T_s) - I_{\nu a}^{\downarrow}(\bar{\theta})], \quad (15)$$

where the ensemble-mean incidence angle, $\bar{\Theta}_i$, of the analytical facet model is calculated from

$$\bar{\Theta}_i = \frac{\int_{\mu_{n1}}^1 \int_0^{\varphi_{n2}} \Theta_i P d\varphi_n d\mu_n}{\int_{\mu_{n1}}^1 \int_0^{\varphi_{n2}} P d\varphi_n d\mu_n} = \int_{\mu_{n1}}^1 \int_0^{\varphi_{n2}} \Theta_i P d\varphi_n d\mu_n, \quad (16)$$

and similarly the local zenith angle of downwelling radiance, $\bar{\theta}$, from

$$\bar{\theta} = \frac{\int_{\mu_{n1}}^1 \int_0^{\varphi_{n2}} \theta P' d\varphi_n d\mu_n}{\int_{\mu_{n1}}^1 \int_0^{\varphi_{n2}} P' d\varphi_n d\mu_n} = \int_{\mu_{n1}}^1 \int_0^{\varphi_{n2}} \theta P' d\varphi_n d\mu_n, \quad (17)$$

where P' is a normalized PDF similar to P except derived without the $\cos(\Theta_i)$ term, which projects wave facet areas normal with the line of sight and is already included in Eq. (16). Eliminating $\cos(\Theta_i)$ from Eqs. (9) and (10) therefore yields

$$P' \equiv \frac{2\mu_0^{-1}\mu_n^{-4}p(\mu_n)}{2\mu_0^{-1}\int_{\mu_{n1}}^1 \mu_n^{-4}p(\mu_n)\varphi_{n2}(\theta_0, \theta_n)d\mu_n}. \quad (18)$$

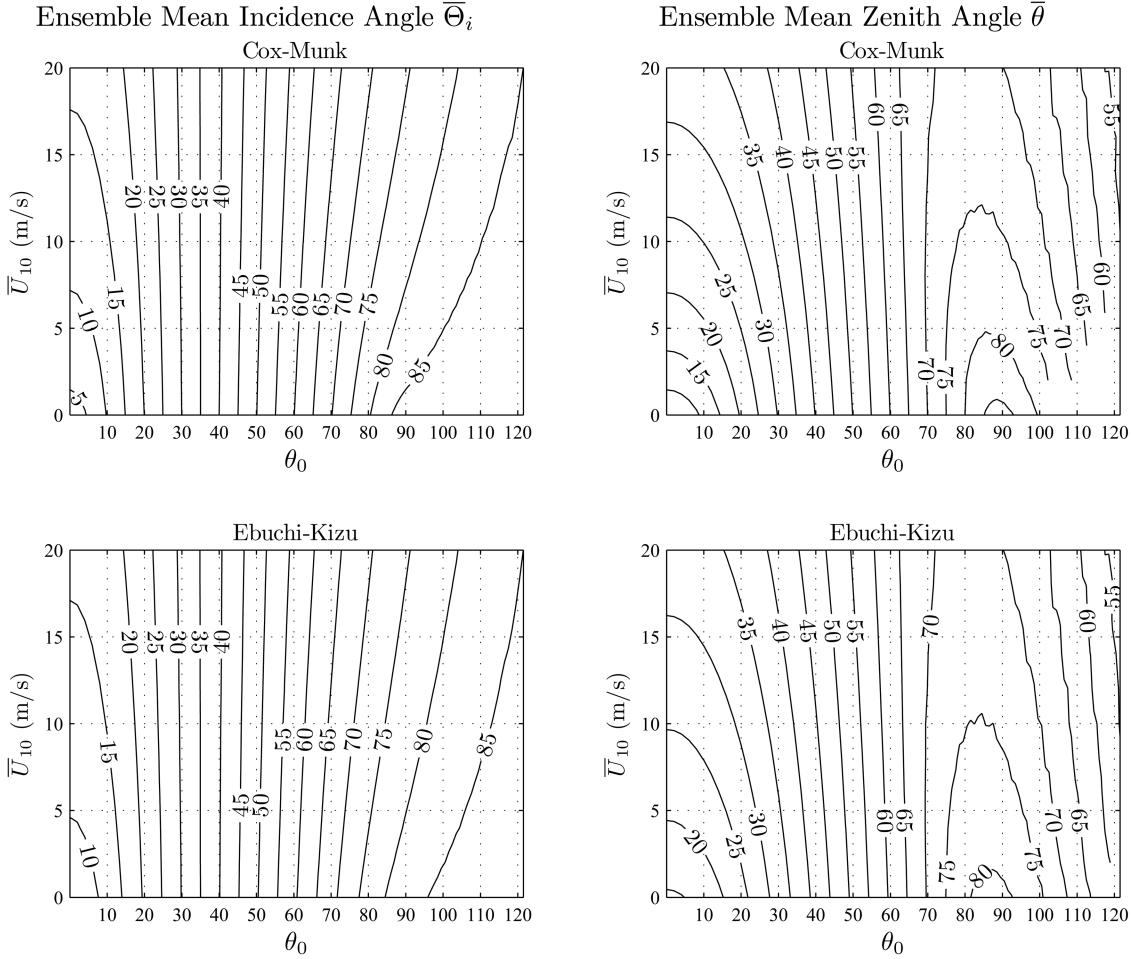


Fig. 2. Ensemble-mean facet geometries for the published mean square slope PDFs of Cox and Munk [15] (top plots) and Ebuchi and Kizu [38] (bottom plots). The left-hand plots show $\bar{\Theta}_i$ calculated from Eq. (16). The right-hand plots show $\bar{\theta}$ calculated from Eq. (17). Note the calculations are extended for observing angles at and below the horizon ($\theta_0 \geq 90^\circ$).

The invariant parameters (viz., N_ν , \bar{U} , and σ^2) in Eqs. (15)–(18) are now implicit for brevity (subscript ν indicates spectral dependence).

We note here, in retrospect, that Hanafin and Minnett [21] present much of their results in terms of the “effective incidence angle” of the rough surface derived from M-AERI measurements for retrieving emissivity. This was, at first, our motivation for deriving Eq. (16) theoretically. We subsequently found that Henderson *et al.* [9] wrote a similar formula (excluding the $\cos(\Theta_i)$ term) to demonstrate the existence of a crossover angle ($\approx 68^\circ$) [1, 4, 5, 9], where increasing \bar{U} increases $\bar{\epsilon}_\nu$.

Using Eqs. (16) and (17), we compute lookup tables (LUTs) of $\bar{\Theta}_i(\theta_0, \bar{U}_{10})$ and $\bar{\theta}(\theta_0, \bar{U}_{10})$, where \bar{U}_{10} is the mean wind speed measured at a 10 m height based upon two published mean square slope PDF models: Cox and Munk [14] and Ebuchi and Kizu [38] (see Appendices A and B for more details). The integrations of Eqs. (16) and (17) are performed using 20-point Gaussian quadrature for both the zenith and azimuth integrals. Our results are summarized as contour plots in θ_0 and \bar{U}_{10} space in Fig. 2 and, for convenience, are tabulated in Tables 1 and 2. Given the

Table 1. Ensemble-Mean Facet Incidence Angle, $\bar{\Theta}_i^a$

θ_0	Wind Speed, \bar{U}_{10} (ms ⁻¹)											
	Cox and Munk [15] PDF					Ebuchi and Kizu [38] PDF						
	0	4	8	12	16	20	0	4	8	12	16	20
0	2.8	7.8	10.5	12.6	14.4	15.9	7.1	9.7	11.6	13.2	14.6	15.9
8	8.3	10.6	12.6	14.4	15.9	17.2	10.2	12.0	13.5	14.9	16.1	17.2
16	16.1	17.0	18.0	19.0	20.0	20.9	16.9	17.7	18.5	19.4	20.1	20.9
24	24.1	24.5	24.9	25.4	25.8	26.3	24.4	24.8	25.1	25.5	25.9	26.3
32	32.0	32.1	32.2	32.4	32.5	32.6	32.1	32.2	32.3	32.4	32.5	32.6
40	40.0	39.8	39.7	39.6	39.5	39.4	39.9	39.8	39.6	39.5	39.4	39.4
48	47.9	47.6	47.2	46.8	46.5	46.1	47.6	47.3	47.0	46.7	46.4	46.1
52.5	52.4	51.9	51.4	50.9	50.4	49.9	52.0	51.5	51.1	50.7	50.3	49.9
56.5	56.4	55.7	55.0	54.4	53.7	53.1	55.8	55.3	54.7	54.2	53.6	53.1
60.5	60.4	59.5	58.7	57.8	57.0	56.3	59.7	58.9	58.2	57.6	56.9	56.3
64.5	64.3	63.3	62.2	61.2	60.2	59.3	63.4	62.5	61.7	60.8	60.1	59.3
68.5	68.3	66.9	65.6	64.4	63.2	62.2	67.2	66.0	65.0	64.0	63.0	62.2
72.5	72.2	70.5	68.8	67.4	66.0	64.8	70.8	69.4	68.1	66.9	65.8	64.8
76.5	76.2	73.8	71.8	70.1	68.6	67.3	74.2	72.5	70.9	69.6	68.4	67.3
80.5	80.0	76.9	74.5	72.6	71.0	69.7	77.3	75.2	73.5	72.1	70.8	69.7
84.5	83.6	79.5	76.9	74.9	73.2	71.8	80.0	77.7	75.8	74.3	73.0	71.8
88.5	86.5	81.6	78.9	76.9	75.2	73.8	82.2	79.7	77.8	76.3	74.9	73.8
92.5	88.1	83.3	80.6	78.6	77.0	75.6	83.9	81.4	79.6	78.0	76.7	75.6
96.5	88.8	84.7	82.1	80.2	78.6	77.2	85.2	82.9	81.1	79.6	78.4	77.2
100.5	90.0	85.7	83.4	81.6	80.1	78.8	86.2	84.1	82.4	81.1	79.9	78.8
104.5	NAN	86.5	84.4	82.7	81.4	80.2	86.9	85.0	83.6	82.3	81.2	80.2
108.5	NAN	87.2	85.4	83.9	82.6	81.5	87.6	85.9	84.6	83.4	82.4	81.5
112.5	NAN	87.9	86.0	84.8	83.6	82.7	88.4	86.6	85.5	84.5	83.4	82.7
116.5	NAN	89.2	86.8	85.7	84.7	83.7	NAN	87.3	86.1	85.2	84.5	83.7
120.5	NAN	NAN	87.6	86.4	85.5	84.6	NAN	88.3	86.9	86.2	85.4	84.6

^a $\bar{\Theta}_i$ are rounded to the nearest tenth of a degree. Not a number (NAN) values occur when $\bar{\Theta}_i \not\leq 90^\circ$, an unphysical result. $\theta_0 > 90^\circ$ are below the horizon. Because of space limitations, wind speeds are subsampled by factor of 2, and observing angles are subsampled by factor of 4.

known variation of reflectance with the incidence angle, these calculations provide physical insights into the mean variation of surface emissivity and specular reflection with surface roughness. The results for the mean incidence angle $\bar{\Theta}_i$ are consistent with the observations of Hanafin and Minnett [21] for $\theta_0 = 55^\circ$, whereby $\bar{\Theta}_i$ is seen to decrease with increasing wind speeds. We observe the crossover angle to be $\approx 35^\circ$ for both PDF models; this value is notably smaller than previous estimates of 68° [4,9]. We have verified that if we exclude the $\cos(\Theta_i)$ term from Eq. (16), as did Henderson *et al.* [9], we also arrive at the 68° crossover angle. Note that neither Eq. (16) nor Eq. (17) require assumptions about multiple reflections—they merely provide the mean surface geometry arising from the distribution of facet inclinations.

Although Eq. (15) models the specular radiance component more accurately than Eq. (3), it does not account for the variations in downwelling atmospheric radiance with θ , which become greater at larger zenith observing angles and wind speeds [4]. To account better for this, we turn to radiative transfer modeling, whereby a new SLR approximation is developed.

2. Radiative Transfer Derived Effective Emissivity and Reflection

Enforcing energy conservation at each wave facet within the FOV of observation, each wave facet's con-

tribution to the radiance field may be broken down into a direct emitted component and a reflected component. The self-consistent analytical facet model RTE for the mean quasi-specular SLR is then written as (e.g., Saunders [33])

$$\bar{R}_{\nu s}(\theta_0) = \int_{\mu_{n1}}^1 \int_0^{\varphi_{n2}} P(\mu_n, \mu_0, \Theta_i) \{[1 - \rho_\nu(\Theta_i)]B_\nu(T_s) + \rho_\nu(\Theta_i)I_{\nu i}(\theta)\} d\varphi_n d\mu_n, \quad (19)$$

$$= \bar{\epsilon}_\nu(\theta_0)B_\nu(T_s) + \int_{\mu_{n1}}^1 \int_0^{\varphi_{n2}} \rho_\nu(\Theta_i)P(\mu_n, \mu_0, \Theta_i)I_{\nu i}(\theta) d\varphi_n d\mu_n, \quad (20)$$

where $\theta = \theta(\mu_n, \mu_0, \Theta_i)$, and $I_{\nu i}(\theta)$ is the surface-incident radiance. The second form of the equation, Eq. (20), shows the RTE in the familiar form consisting of an emission term and a reflection term, which arises from $B_\nu(T_s)$ remaining constant with the facet angle. It becomes obvious that if one uses rough surface emissivity model calculations based on Eqs. (6) and (14) for radiative transfer applications, the reflection is properly given by the second term in Eq. (20) [8]. Using the specular approximation,

Table 2. Ensemble-Mean Zenith Incidence Angle, $\bar{\theta}^a$

θ_0	Wind Speed, \bar{U}_{10} (ms ⁻¹)											
	Cox and Munk [15] PDF					Ebuchi and Kizu [38] PDF						
	0	4	8	12	16	20	0	4	8	12	16	20
0	5.6	15.6	21.3	25.6	29.3	32.5	14.4	19.5	23.5	26.9	29.8	32.5
8	9.4	17.1	22.4	26.5	30.1	33.2	16	20.8	24.5	27.8	30.6	33.2
16	16.6	21.3	25.6	29.2	32.4	35.2	20.5	24.2	27.4	30.3	32.8	35.2
24	24.4	27.3	30.4	33.3	36.0	38.5	26.8	29.4	31.9	34.2	36.4	38.5
32	32.3	34.3	36.5	38.6	40.8	42.8	33.9	35.7	37.6	39.4	41.1	42.8
40	40.2	41.7	43.2	44.8	46.4	48.1	41.4	42.7	44.0	45.4	46.7	48.0
48	48.2	49.2	50.4	51.5	52.7	54.0	49.1	50.0	51.0	51.9	52.9	54.0
52.5	52.6	53.6	54.5	55.5	56.5	57.5	53.4	54.2	55.0	55.8	56.6	57.5
56.5	56.6	57.4	58.2	59.0	59.8	60.6	57.3	57.9	58.6	59.3	60.0	60.6
60.5	60.6	61.3	62.0	62.6	63.2	63.6	61.2	61.7	62.3	62.8	63.3	63.6
64.5	64.6	65.2	65.7	66.0	66.2	66.3	65.1	65.5	65.9	66.1	66.2	66.3
68.5	68.6	69.0	69.3	69.2	68.8	68.5	69.0	69.3	69.3	69.2	68.8	68.5
72.5	72.6	72.9	72.5	71.8	70.9	70.3	72.8	72.7	72.3	71.5	70.8	70.3
76.5	76.5	76.4	75.2	73.6	72.5	71.0	76.5	75.6	74.4	73.2	72.3	71.0
80.5	80.5	79.0	76.7	74.8	73.1	71.3	79.6	77.6	75.7	74.3	72.7	71.3
84.5	84.4	80.4	77.5	75.1	72.8	71.0	81.3	78.3	76.3	74.2	72.5	71.0
88.5	86.7	80.5	77.0	74.3	72.2	70.4	81.3	78.0	75.6	73.6	71.9	70.4
92.5	85.3	79.3	75.7	73.0	71.1	69.3	80.1	76.8	74.3	72.3	70.8	69.3
96.5	82.3	77.2	74.3	71.5	69.3	67.5	78.0	75.2	72.8	70.7	68.9	67.5
100.5	79.4	74.5	71.4	69.8	67.5	65.6	75.5	72.7	70.9	69.0	67.2	65.6
104.5	NAN	71.6	69.5	67.4	65.6	63.6	72.1	69.3	67.8	66.9	65.2	63.6
108.5	NAN	68.7	66.0	64.3	63.3	61.5	69.0	67.4	65.7	63.3	63.0	61.5
112.5	NAN	65.1	63.1	62.1	60.3	59.3	65.9	64.2	62.1	61.2	60.5	59.3
116.5	NAN	62.3	60.4	58.3	57.3	56.9	NAN	60.8	59.7	58.7	56.8	56.9
120.5	NAN	NAN	56.5	56.0	55.0	53.2	NAN	57.7	56.5	55.2	54.7	53.1

^a θ are rounded to the nearest tenth of a degree. NAN values occur when $\bar{\theta}_i < 90^\circ$, an unphysical result (see Table 1). $\theta_0 > 90^\circ$ are below the horizon. Because of space limitations, wind speeds are subsampled by factor of 2, and observing angles are subsampled by factor of 4.

Eq. (3), for this purpose results in nonnegligible bias [4,8], as will be demonstrated empirically in Part II.

As prescribed by Eq. (20), the calculation of $\bar{R}_{ls}(\theta_0)$ requires knowledge of surface-incident radiance, $I_{vi}(\theta)$. To illustrate our formulation of this, Fig. 1 shows a ray-trace schematic that summarizes the sources of SLR to be accounted for. In modeling the surface-incident radiance, $I_{vi}(\theta)$ in Eq. (19), it is realized that the magnitude depends first on the origin of the facet-incident rays (i.e., either from the surface or the sky). Previous investigators [4,5,8] assumed a hypothetical “cutoff angle” as the point below which rays no longer originate from the surface, assuming a parabolic decay [5] for intermediate angles between this angle and 90° . In the present work, however, we apply a more recent method proposed by Masuda [12], defining the probability of a ray originating from the surface as

$$p_s(\theta, \sigma^2) \equiv \begin{cases} 1 - S(\theta, \sigma^2), & \theta < \pi/2 \\ 1, & \theta \geq \pi/2 \end{cases}, \quad (21)$$

where $S(\theta, \sigma^2)$ is the Saunders [32,33] shadowing factor. From physical reasoning, Masuda pointed out that the shadowing factor, by reciprocity, is also the probability that a surface-incident ray does not originate from another facet [12]. It is convenient here to calculate $S(\theta, \sigma^2)$ using Saunders’ analytical

solution, that is Eqs. (11) and (12), rather than Eq. (9), which requires numerical quadrature. Figure 3 shows the resulting variation of p_s versus surface wind speed and facet incidence angle, θ . Incident rays originate from the sky when $p_s(\theta, \sigma^2) = 0$ (the most common case) from the surface when $p_s(\theta, \sigma^2) = 1$ or from either one when $0 < p_s(\theta, \sigma^2) < 1$. The results in Fig. 3 are largely consistent with the range of cutoff angles identified by Watts *et al.* [4], 79° – 89.1° , although the angle evidently dips below this range at higher wind speeds. Unlike previous methods, however, this method is physically consistent with the chosen shadowing model, and it accounts for a variable cutoff angle between sea and sky, which, physically speaking, should decrease with surface roughness.

Incident rays originating from the surface may either be emitted (SESR) or reflected (surface-reflected, surface-reflected, SRSR) [4] from other wave facets. The SESR effect is larger than SRSR and easier to treat, because it is assumed that the surface temperature does not change appreciably, and thus equations of the form of Eq. (13) may be derived. Multiple reflections of sky radiance (i.e., involving two or more surface reflections), though second order, are much more difficult to treat analytically, given that the sky radiance varies substantially with zenith angle, and the wave-slope distribution for the

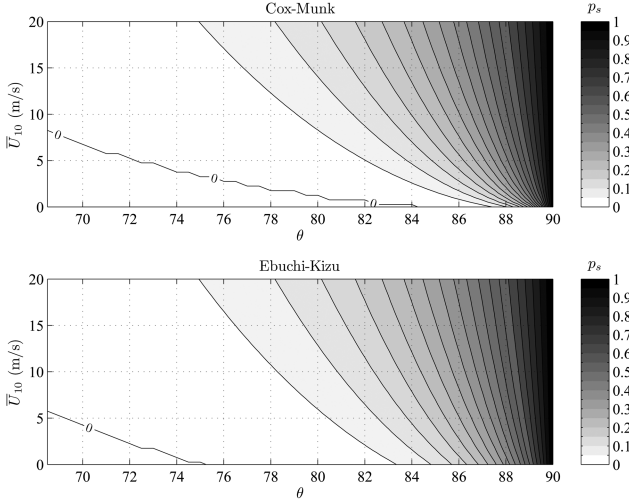


Fig. 3. Probability of a facet-incident ray originating from surface, $p_s(\theta, \sigma^2)$, defined by Eq. (21) versus the mean surface wind speed, \bar{U}_{10} , and facet incidence angle, θ .

FOVs of wave facets differs from the empirical values [14,38]. Based on their Monte Carlo simulations, Henderson *et al.* [9] modeled up to ten reflections and found that the number of possible reflections is generally $\lesssim 5$, but they do not provide details on the relative contributions of each successive reflection. In previous analytical models, higher-order reflections have been roughly estimated to be negligible [4,5,11]. In the present work we approximate double reflections of sky radiance through the use of Eqs. (16) and (17), assuming the mean geometry of the surface does not vary appreciably with FOV surface area in the limit of multiple FOVs. We subsequently find in model calculations (see Section 3) that double reflections of sky radiance, while small, may not be completely negligible, particularly in quasi-opaque atmospheres.

Referring back to Fig. 1, the surface-incident radiance is thus modeled as follows:

$$I_{\nu i}(\theta) = [1 - p_s(\theta, \sigma^2)]I_{\nu a}^\downarrow(\theta) + p_s(\theta, \sigma^2)[I_{\nu se}(\pi - \theta) + I_{\nu sr}(\pi - \theta)], \quad (22)$$

where p_s is defined by Eq. (21), $I_{\nu a}^\downarrow(\theta)$ is computed from Eq. (2), and the mean surface emission and reflected sky radiance from other wave facets, $I_{\nu se}$ and $I_{\nu sr}$, respectively, are approximated as

$$I_{\nu se}(\pi - \theta) \approx \{1 - \rho_\nu[\bar{\Theta}_i(\pi - \theta)]\}B_\nu(T_s), \quad (23)$$

$$I_{\nu sr}(\pi - \theta) \approx \rho_\nu[\bar{\Theta}_i(\pi - \theta)]I_{\nu a}^\downarrow(\bar{\theta}(\pi - \theta)). \quad (24)$$

Inserting Eqs. (22)–(24) into Eq. (19) and defining the SESR-enhanced emissivity to be

$$\epsilon_\nu^+(\theta) \equiv [1 - \rho_\nu(\Theta_i)] + \rho_\nu(\Theta_i)p_s(\theta, \sigma^2)\{1 - \rho_\nu[\bar{\Theta}_i(\pi - \theta)]\}, \quad (25)$$

renders the full model RTE [Eq. (19)], including SESR and SRSR effects, in the two-term form

$$\begin{aligned} \bar{R}_{\nu s}(\theta_0) &= \bar{\epsilon}_\nu^+(\theta_0)B_\nu(T_s) \\ &+ \int_{\mu_{n1}}^1 \int_0^{\varphi_{n2}} \rho_\nu(\Theta_i)P(\mu_n, \mu_0, \Theta_i)\{I_{\nu a}^\downarrow(\theta) \\ &- p_s(\theta, \sigma^2)[I_{\nu a}^\downarrow(\theta) - I_{\nu sr}]\}d\varphi_n d\mu_n. \end{aligned} \quad (26)$$

We note that Eq. (26) constitutes an accurate analytical model for calculating the mean IR SLR, $\bar{R}_{\nu s}$, including an approximation for double reflections of downwelling atmospheric radiances. Numerical integration of Eq. (26) can be performed using a suitable uplooking transmittance model and multipoint Gaussian quadrature [8]. However, it is presumed that such a calculation (involving a double integral of downwelling radiances with varying integration limits, namely $\varphi_{n2}(\theta_0, \theta_n)$ and $\mu_{n1}(\bar{U}_{10})$) is simply impractical for operational processing systems (at least in the near term). Both Watts *et al.* [4] and Nalli *et al.* [8] attempted to address this problem by introducing approximations for the double integral. The latter sought to achieve this for hyperspectral data by introducing a reflection-diffusivity angle [8]. Unfortunately, even the diffusivity approximation is still not convenient for routine use since the LUT depends on concurrent column transmittances (and hence is specific to transmittance model and instrument channel response functions), and is then applicable only to window channels. Thus, it remains for us to find a practical, yet suitably accurate, approximation to Eq. (26) that lends itself toward convenient implementation within a wide variety of remote sensing applications.

We proceed by first considering that the predominant means for measuring IR SLR and emissivity in the field has been through M-AERI FTS measurements [20]. Since the ultimate goal is to model the observed behavior, it is logical to propose a solution based on a direct application of the emissivity retrieval methodology [16,21] to our model. This is achieved by assuming SLR, modeled by Eq. (26), can be sufficiently well-approximated as

$$\epsilon_\nu(\theta_0)B_\nu(T_s) + [1 - \epsilon_\nu(\theta_0)]I_{\nu a}^\downarrow(\theta_0) \approx \bar{R}_{\nu s}(\theta_0), \quad (27)$$

where we define an effective emissivity, ϵ_ν , corresponding to the effective incidence angle of the wave facets, Θ_{ie} , to be

$$\epsilon_\nu(\theta_0, \bar{U}_{10}, N_\nu) \equiv 1 - \rho[\Theta_{ie}(\theta_0, \bar{U}_{10}), N_\nu]. \quad (28)$$

From Eqs. (27) and (28), one may see that Θ_{ie} is analogous to $\bar{\Theta}_i$ in Eq. (15), except that Θ_{ie} is to be derived from radiative transfer in Eq. (27) rather than from the mean ray geometry as in Eq. (16). While at first glance this may seem no different from the standard approach based on Eq. (3), recall that Eq. (3) requires *a priori* computations of emissivity based on Eq. (14),

whereas we propose that $\varepsilon_\nu(\theta_0)$ may be derived in Eq. (27) such that the full quasi-specular radiance calculated from Eq. (26) is closely approximated. In so doing, we hypothesize that the downwelling radiance at the emission angle, $I_{\nu a}^\downarrow(\theta_0)$, provides sufficient information about the atmospheric contribution, and that a small perturbation about this value arising from an integral about θ_0 , in a mean sense, can be aliased as emissivity. We comment here that because the spectral and angular characteristics of wave facet emissivity are fundamentally determined by the electromagnetic properties of the fluid, that is, Eqs. (4) and (5), any consideration of wind speed dependence (i.e., the geometry of multiple wave slopes within an observer FOV) is implicitly a study of effective emissivity. This includes facet models of the form of Eq. (14); Yoshimori *et al.* [2,3], for example, also used this terminology.

Solving Eqs. (27) and (28) for $B_\nu(T_s)$, then taking the inverse Planck function yields [16,21,39]

$$T_{\nu s}(\Theta_{ie}) = B_\nu^{-1} \left(\frac{\bar{R}_{\nu s}(\theta_0) - \rho_\nu(\Theta_{ie}) I_{\nu a}^\downarrow(\theta_0)}{1 - \rho_\nu(\Theta_{ie})} \right). \quad (29)$$

Because the thermodynamic skin temperature, T_s , is not correlated with spectral features characteristic of atmospheric emission, any such features found in $T_{\nu s}$ originate from an incorrect value of ρ_ν . The correct value is retrieved by iterating the effective incidence angle, Θ_{ie} , until the spectral variance is minimized [16,21,39]:

$$\frac{1}{n-1} \sum_\nu [T_{\nu s}(\Theta_{ie}) - \bar{T}_s(\Theta_{ie})]^2 = \min, \quad (30)$$

where n is the number of spectral channels. Equations (29) and (30) form the basis for retrieving emissivity from M-AERI over small wavenumber intervals [21] when T_s is unknown (the method is coined VarMinT in Ref. [21]). In this work Θ_{ie} is arrived at via a similar minimization technique, that is,

$$\frac{1}{n-1} \sqrt{\sum_\nu \delta T_{B_\nu}(\Theta_{ie})^2} = \min, \quad (31)$$

where, from Eqs. (27) and (28),

$$\begin{aligned} \delta T_{B_\nu}(\Theta_{ie}) &= B_\nu^{-1} \{ [1 - \rho_\nu(\Theta_{ie})] B_\nu(T_s) + \rho_\nu(\Theta_{ie}) I_{\nu a}^\downarrow(\theta_0) \} \\ &\quad - B_\nu^{-1} \{ \bar{R}_{\nu s}(\theta_0) \}, \end{aligned} \quad (32)$$

with $\bar{R}_{\nu s}(\theta_0)$ being the modeled true quasi-specular radiance spectrum calculated from Eq. (26). The Fresnel reflectivity, ρ_ν , is then calculated for value of Θ_{ie} obtained from the minimization.

Because Eqs. (29) and (30) also assume radiative transfer based on approximation Eq. (27), we note that, as a corollary, the emissivity parameter retrieved by M-AERI also constitutes an effective

emissivity, ε_ν , as we have defined it. Our radiative transfer-based minimization, Eqs. (31) and (32), assumes that the spectral variation of ε_ν may be derived theoretically from Eq. (5) for a given set of refractive indices. The minimization is thus extended to much larger spectral intervals, which then renders the computed value of Θ_{ie} valid for the entire IR spectrum. We found that a minimization over a spectral region encompassing the shortwave IR (SWIR) and LWIR atmospheric windows, namely $850\text{--}1315\text{ cm}^{-1}$ and $2017\text{--}2664\text{ cm}^{-1}$, works well for capturing a range of atmospheric transmittance. Our rationale for this spectral subsample is to omit opaque absorption bands (viz., H_2O and CO_2) as well as to avoid sharp spectral changes in the Fresnel reflection coefficient (viz., $\nu \lesssim 850\text{cm}^{-1}$ and $1500 \lesssim \nu \lesssim 1800\text{ cm}^{-1}$). Note that we have verified that both minimization techniques, VarMinT Eqs. (29) and (30) and our Eqs. (31) and (32), yield nearly identical results with only slight differences occurring at $\theta_0 \gtrsim 65^\circ$, well outside the range where M-AERI generally operates.

3. Model Calculations

Based on Eqs. (26)–(28), (31), and (32), we compute $\Theta_{ie}(\theta_0, \bar{U}_{10})$ for the two published wave slope PDFs [15,38]. The specific steps taken to achieve this are summarized below.

A. Methodology

Atmospheric-emitted downwelling radiances, $I_{\nu a}^\downarrow(\theta)$, are calculated from the Clough *et al.* [40] line-by-line RTM (LBLRTM) (v9.4) then convolved and apodized to AERI resolution ($\approx 0.5\text{ cm}^{-1}$) using code developed by D. Tobin (University of Wisconsin–Madison). To ensure a realistic range of marine atmospheric transmittance (in addition to the substantial spectral

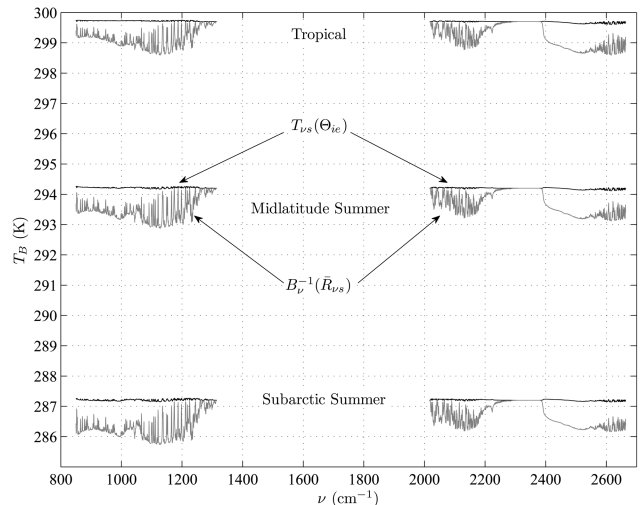


Fig. 4. Example of spectral minimizations for the three training atmospheres ($\bar{U}_{10} = 10\text{ ms}^{-1}$, $\theta_0 = 55^\circ$, Ebuchi and Kizu [38] slope PDF, and Hale and Querry [42] refractive indices). The true T_s for tropical, midlatitude summer, and subarctic summer atmospheres were set at 299.7 K , 294.2 K , and 287.2 K , respectively.

Effective Incidence Angle Θ_{ie} – Cox-Munk Wave Slope PDF

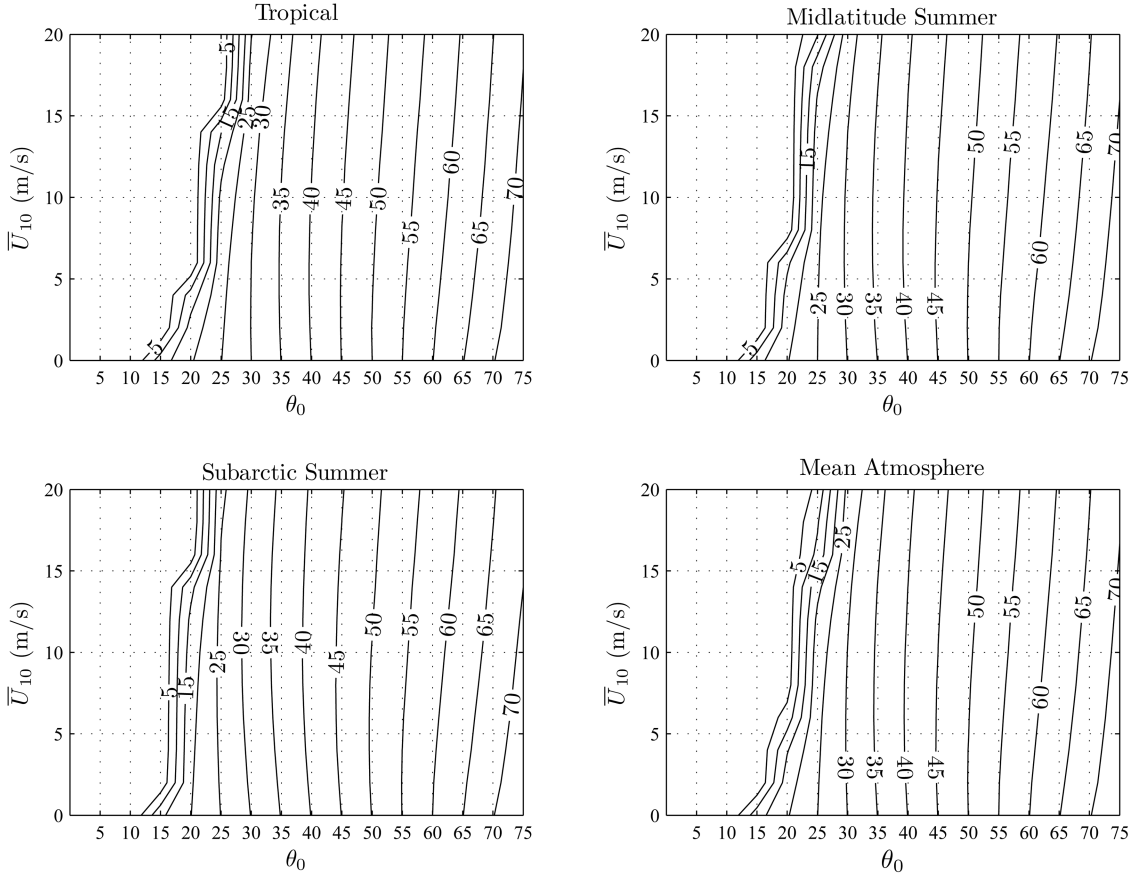


Fig. 5. Derived effective incidence angle of ocean surface waves (mean of six published refractive indices) for the Cox and Munk [15] wave slope PDF. The top two and lower left-hand panels show the results for the individual atmospheres with the bottom right-hand panel showing the mean of these as the final result tabulated in Table 3.

variation already present in a given atmosphere), calculations are run for the LBLRTM tropical, midlatitude summer, and subarctic summer model atmospheres (these all have above-freezing temperatures in their lowest layers), along with boundary layer aerosols defined by the Navy maritime model default settings. We again use Gaussian quadrature for the accurate numerical integration of Eq. (26) (10- and 16-point for the zenith and azimuth angles, respectively), computing the wind-roughened SLR spectra of the three sample atmospheres for θ_0 up to 75° and \bar{U}_{10} up to 20 ms^{-1} .

In all cases the $T_{vs}(\Theta_{ie})$ derived from Eq. (29) based on Θ_{ie} from Eqs. (31) and (32) converges to within $\approx 0.05\text{ K}$ of the true T_s , which was set equal to the lowest layer air temperature in each model atmosphere. Examples of this are shown in Fig. 4 for the three model atmospheres and $\bar{U}_{10} = 10\text{ ms}^{-1}$ and $\theta_0 = 55^\circ$.

Strictly speaking the derived Θ_{ie} has a residual dependence on the refractive indices used in the calculation. Although this dependence is deemed negligible, we nevertheless suppress any residual dependence by repeating the calculations for a set

of six published refractive indices for pure water (Pontier and Dechambenoit [41], Hale and Querry [42], Downing and Williams [43], Segelstein [44], Wieliczka *et al.* [45], and Bertie and Lan [46]), then simply taking the mean, $\bar{\Theta}_{ie}$. As with previous works, we apply the salinity correction of Friedman [47] to these datasets to approximate the refractive index for ocean water. Note here that the effects of salinity deviating from Friedman's concentrations (34.5 ppt; chlorinity 19.0 ppt) have been deemed negligible [8,28], so it is not necessary to recompute the values of Θ_{ie} for varying salinities.

B. Results and Discussion

The final results of $\bar{\Theta}_{ie}(\theta_0, \bar{U}_{10})$ for the Cox–Munk and Ebuchi–Kizu wave slope PDFs are summarized as contour plots in Figs. 5 and 6, respectively, and for convenience are given as a two-part LUT in Table 3. Figures 5 and 6 reveal that the results for the three atmospheres do not differ substantially from one another. The largest variations among them are found at the smaller angles $\theta_0 \lesssim 40^\circ$. However, the Fresnel reflection coefficient varies slowly over these angles, so these differences are completely negligible in

Effective Incidence Angle Θ_{ie} – Ebuchi-Kizu Wave Slope PDF

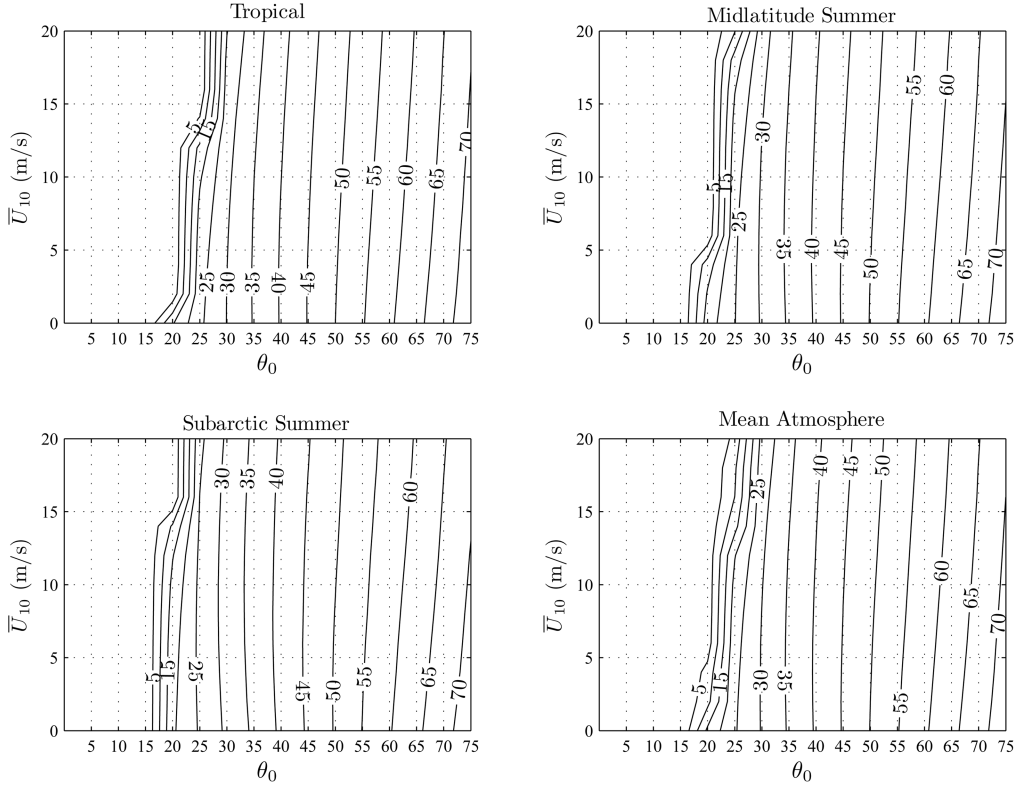


Fig. 6. Similar to Fig. 5 though for the Ebuchi and Kizu [38] wave slope PDF instead.

Table 3. Mean Effective Incidence Angle, $\bar{\Theta}_{ie}^a$

θ_0	Wind Speed, \bar{U}_{10} (ms^{-1})										
	0	2	4	5	8	10	12	14	16	18	20
Cox and Munk [15] PDF											
15	13.0	0.1	0.0	0.0	0.0	0.0	0.0	0.0	0.0	0.0	0.0
20	19.6	17.8	14.6	7.1	2.5	1.8	1.7	1.4	0.2	0.0	0.0
25	25.0	24.7	24.4	24.0	23.4	22.6	21.2	18.6	11.3	9.3	6.2
30	30.1	30.3	30.4	30.4	30.3	30.1	29.7	29.3	28.6	27.8	26.6
35	35.1	35.4	35.6	35.7	35.7	35.6	35.4	35.1	34.7	34.2	33.7
40	40.1	40.4	40.6	40.6	40.6	40.5	40.3	40.0	39.8	39.4	39.1
45	45.1	45.3	45.4	45.4	45.2	45.1	44.8	44.6	44.3	43.9	43.6
50	50.0	50.1	50.1	49.9	49.7	49.4	49.1	48.8	48.5	48.2	47.9
55	55.0	54.9	54.6	54.4	54.0	53.7	53.4	53.1	52.8	52.4	52.1
60	59.9	59.6	59.1	58.7	58.3	57.9	57.6	57.2	56.8	56.5	56.2
65	64.8	64.2	63.5	63.1	62.5	62.1	61.7	61.3	61.0	60.7	60.4
70	69.7	68.7	68.1	67.5	67.0	66.6	66.2	65.8	65.4	65.1	64.8
Ebuchi and Kizu [38] PDF											
15	0.0	0.0	0.0	0.0	0.0	0.0	0.0	0.0	0.0	0.0	0.0
20	16.1	8.5	6.5	2.3	1.8	1.7	1.5	1.1	0.0	0.0	0.0
25	24.5	24.3	23.9	23.3	22.6	21.5	19.7	13.4	10.0	9.1	6.2
30	30.3	30.4	30.4	30.3	30.1	29.8	29.4	29.0	28.3	27.6	26.6
35	35.5	35.7	35.7	35.7	35.6	35.5	35.2	34.9	34.5	34.1	33.7
40	40.5	40.6	40.7	40.6	40.5	40.3	40.1	39.9	39.6	39.4	39.1
45	45.4	45.4	45.3	45.2	45.1	44.9	44.7	44.4	44.2	43.9	43.6
50	50.1	50.0	49.8	49.6	49.4	49.2	48.9	48.7	48.4	48.2	47.9
55	54.7	54.5	54.3	54.0	53.7	53.4	53.2	52.9	52.7	52.4	52.1
60	59.3	58.9	58.5	58.3	57.9	57.6	57.3	57.0	56.7	56.4	56.2
65	63.7	63.3	62.9	62.5	62.1	61.8	61.5	61.2	60.9	60.6	60.4
70	68.3	67.7	67.3	66.9	66.6	66.2	65.9	65.6	65.3	65.1	64.8

^a Θ_{ie} are rounded to the nearest tenth of a degree. Note that $\bar{\Theta}_{ie} = 0.0$ for $\theta_0 = \{0^\circ, 5^\circ, 10^\circ\}$ over the range of wind speeds.

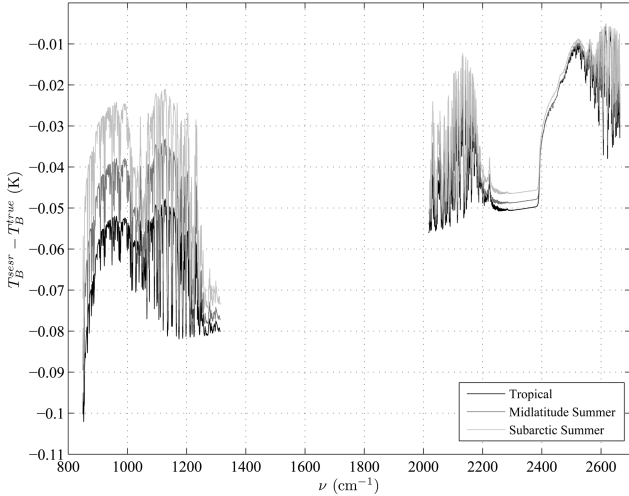


Fig. 7. Approximate magnitude of SRSR contribution to the SLR ($\bar{U}_{10} = 10 \text{ ms}^{-1}$, $\theta_0 = 55^\circ$, Ebuchi and Kizu [38] slope PDF, and Hale and Querry [42] refractive indices).

emissivity. More critically at the larger angles, $\theta_0 \gtrsim 45^\circ$, the patterns and magnitudes are quite similar among the three atmospheres, so by taking a zonally weighted mean, we obtain a result that spans a range of atmospheric transmittance (lower right panel). It is interesting to note that the values of Θ_{ie} at $\theta_0 \gtrsim 50^\circ$ are similar to the ensemble-mean angle $\bar{\Theta}_i$ obtained from Eq. (16) (compare with the left panels of Fig. 2).

Recall that the full SLR model Eq. (26) included self-consistent approximations for SESR and SRSR radiance contributions. To provide some sense of the magnitude of the SRSR contribution to the total SLR, Fig. 7 plots the difference in surface brightness temperature between calculations including SESR-only contributions and calculations including both SESR and SRSR. It can be seen that the modeled SRSR contribution depends heavily on the atmospheric opacity. In absorption bands, the contributions are larger but are of less consequence, because the transmittance between the observer and the surface approaches zero. More notable,

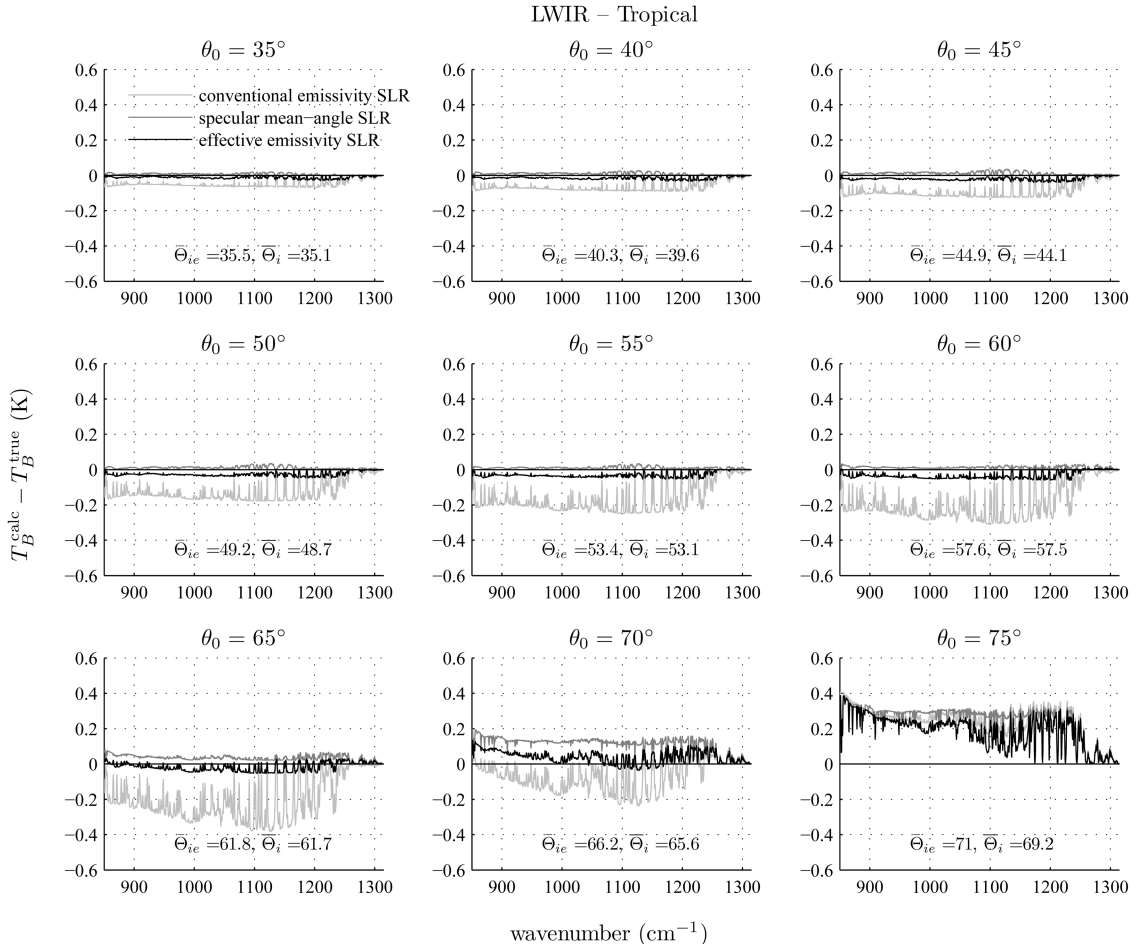


Fig. 8. Simulated SLR brightness temperature calc – true ($T_B^{\text{calc}} - T_B^{\text{true}}$) in the LWIR window for the tropical model atmosphere. As with previous figures, the results are shown for $\bar{U}_{10} = 10 \text{ ms}^{-1}$, the Ebuchi and Kizu [38] slope PDF, and Hale and Querry [42] refractive indices. The blue curves show the results using the conventional SLR model, Eqs. (3) and (14), the magenta curves show the results using the specular ensemble-mean angle SLR model, Eqs. (15)–(17), and the red curves show the results using the effective emissivity and reflection SLR model, Eqs. (27) and (28).

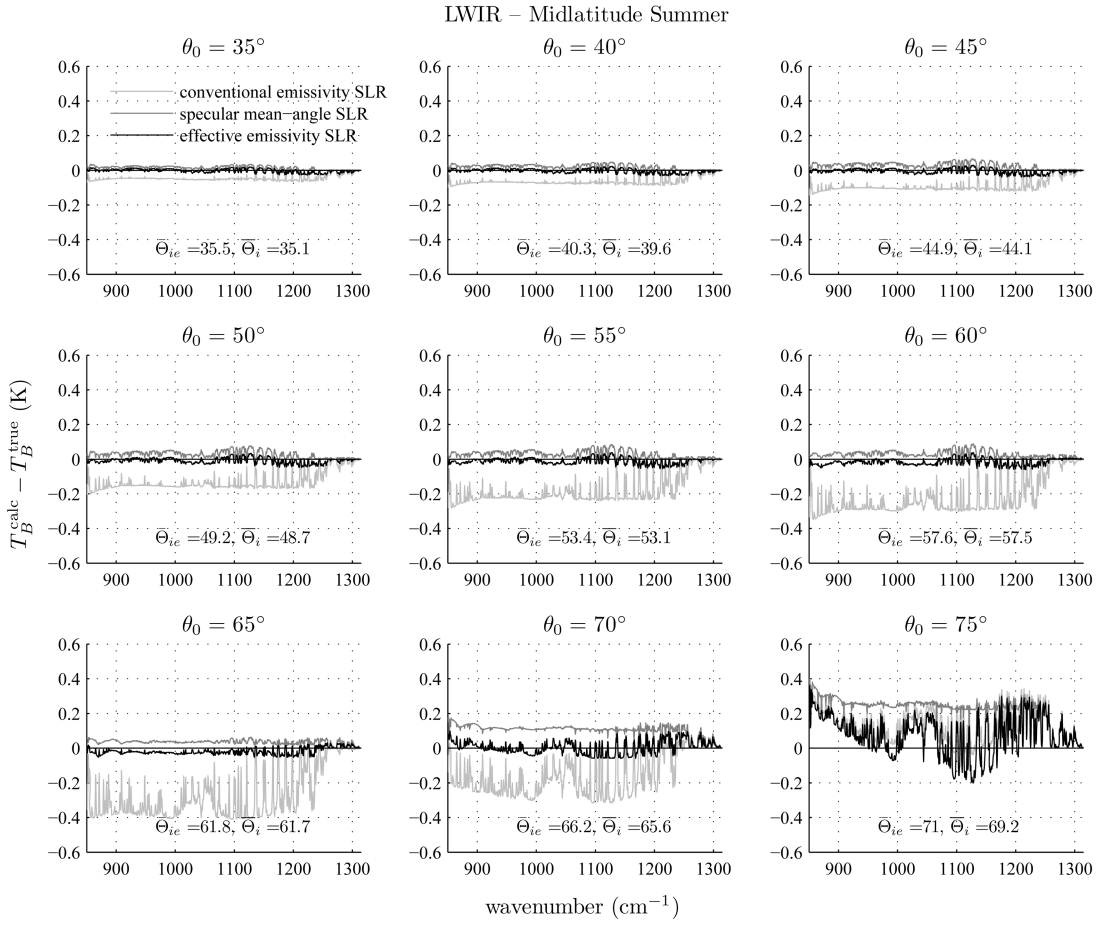


Fig. 9. Similar to Fig. 8 though for the midlatitude summer model atmosphere instead.

therefore, are the spectral microwindows in the LWIR window regions (viz., $\simeq 800\text{--}1000$ and $1070\text{--}1170\text{ cm}^{-1}$), where the SRSR contribution is seen to vary between 0.02 and 0.09 K. Only in the SWIR superwindows ($2500\text{--}2700\text{ cm}^{-1}$) can the magnitudes be deemed completely negligible.

Given the values of $\Theta_{ie}(\theta_0, \bar{U}_{10})$ in Table 3, one can conveniently calculate the effective emissivity, ε_ν , for any of the given set of water refractive indices [41–46] from Eq. (28). Given ε_ν along with a single downwelling calculation, $I_{la}^\downarrow(\theta_0)$, the wind-roughened SLR, $R_{ls}(\theta_0)$, is then easily computed from Eq. (27).

To provide a theoretical assessment of our proposed methodology, we simulate brightness temperature “calculation minus truth” (calc – true), where the calculation is obtained from the methodology, and the truth is simulated from the full hemispheric integration in Eq. (26). For reference we also compute calc – true for the conventional approximation, Eqs. (3) and (14), and the ensemble-mean angle approximation developed in Section 2, Eqs. (15)–(17). Spectral results for the three model atmospheres and 10 ms^{-1} wind speed in the LWIR window are plotted in Figs. 8–10 and the SWIR window in Figs. 11–13. Contour plots of the variation of the LWIR and SWIR spectral bias and variability as

functions of observing angle and wind speed for the tropical atmosphere are given in Figs. 14 and 15. The results presented in these figures are discussed and summarized in the following paragraphs.

First the conventional one-stream model, Eqs. (3) and (14), consistently underestimates microwindow observations for zenith observing angles $40^\circ \lesssim \theta_0 \lesssim 70^\circ$. The magnitude of the bias generally increases with zenith angle and wind speed up to a crossover angle somewhere between 65° and 70° (Fig. 14, top plots). The crossover angle corresponds to the angle at which conventional emissivity models [4,5,9,12] begin to show increasing emissivity with wind speed. The shift from negative to positive bias at these angles is most pronounced in the tropical atmosphere (compare Figs. 8–10). This result is consistent with Nalli *et al.* [8] who found that the reflection-diffusivity angle decreases with wind speed to $<\theta_0$ at these angles in moist atmospheres. This means that in these circumstances, the downwelling radiances become less than those at θ_0 . The biases are most negative in the LWIR window, reaching -0.4 K at 65° in the more transparent atmospheres (see Figs. 9 and 10). In the SWIR window, although the downwelling radiances are considerably less, the biases can still reach -0.2 K (see Figs. 11–13,

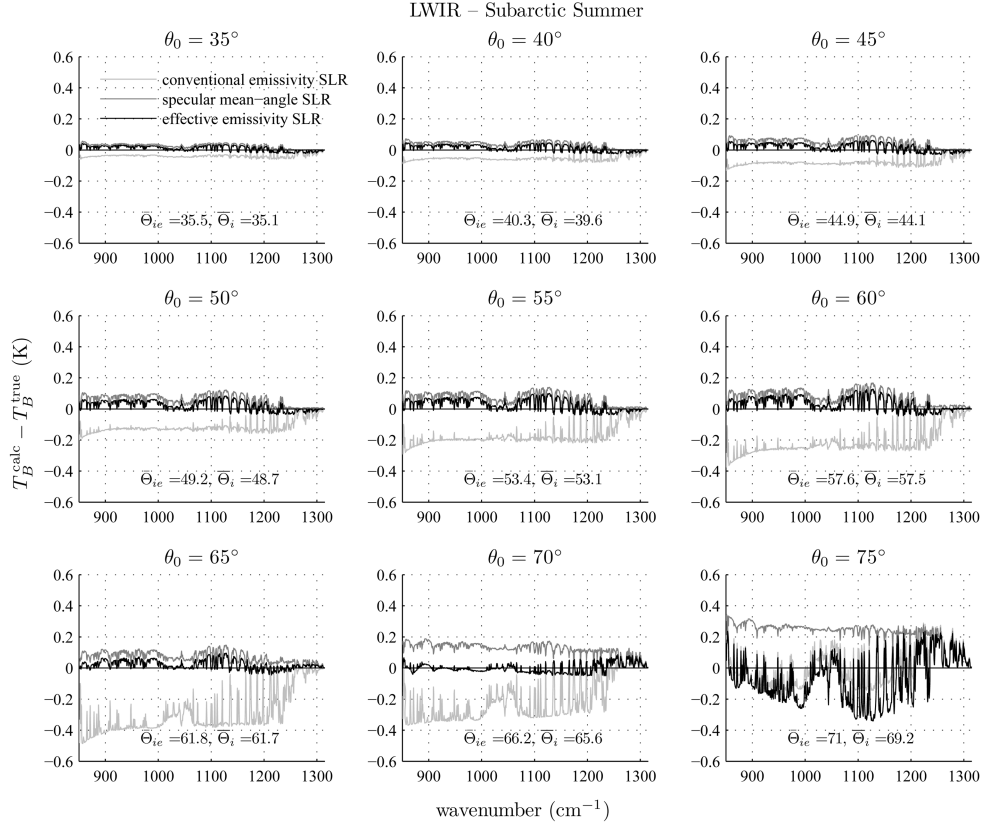


Fig. 10. Similar to Fig. 8 though for the subarctic summer model atmosphere instead.

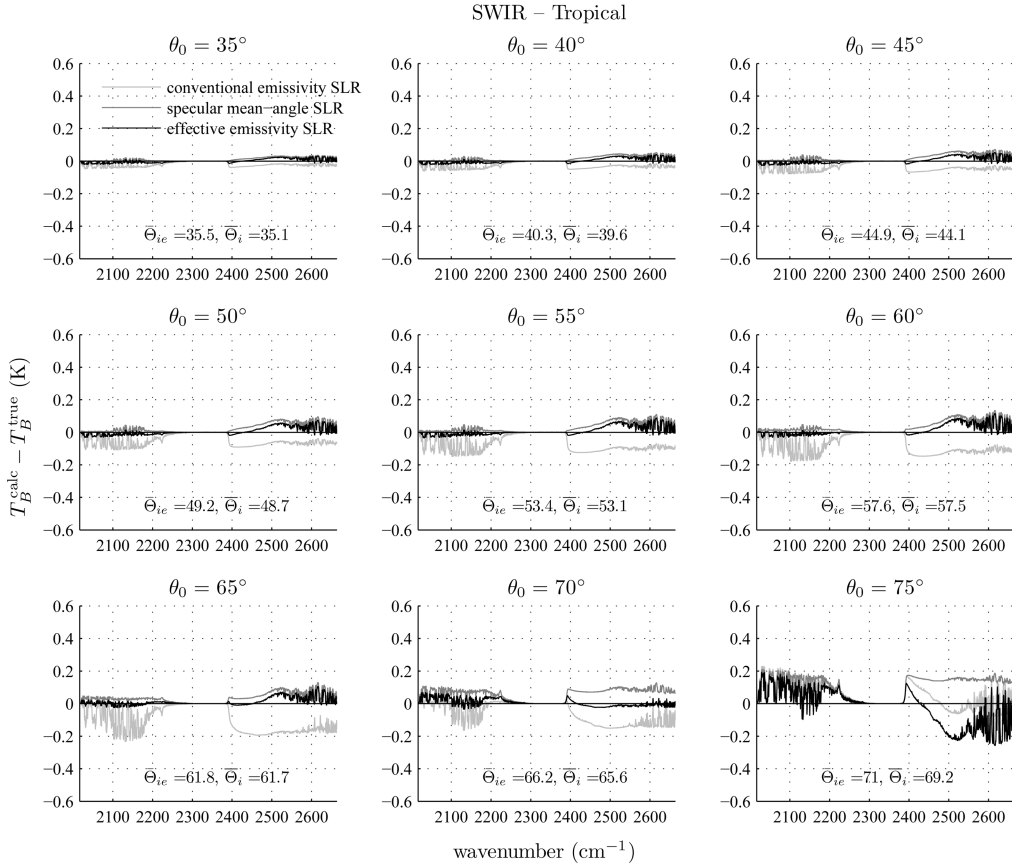


Fig. 11. Similar to Fig. 8 though for the SWIR window regions instead.

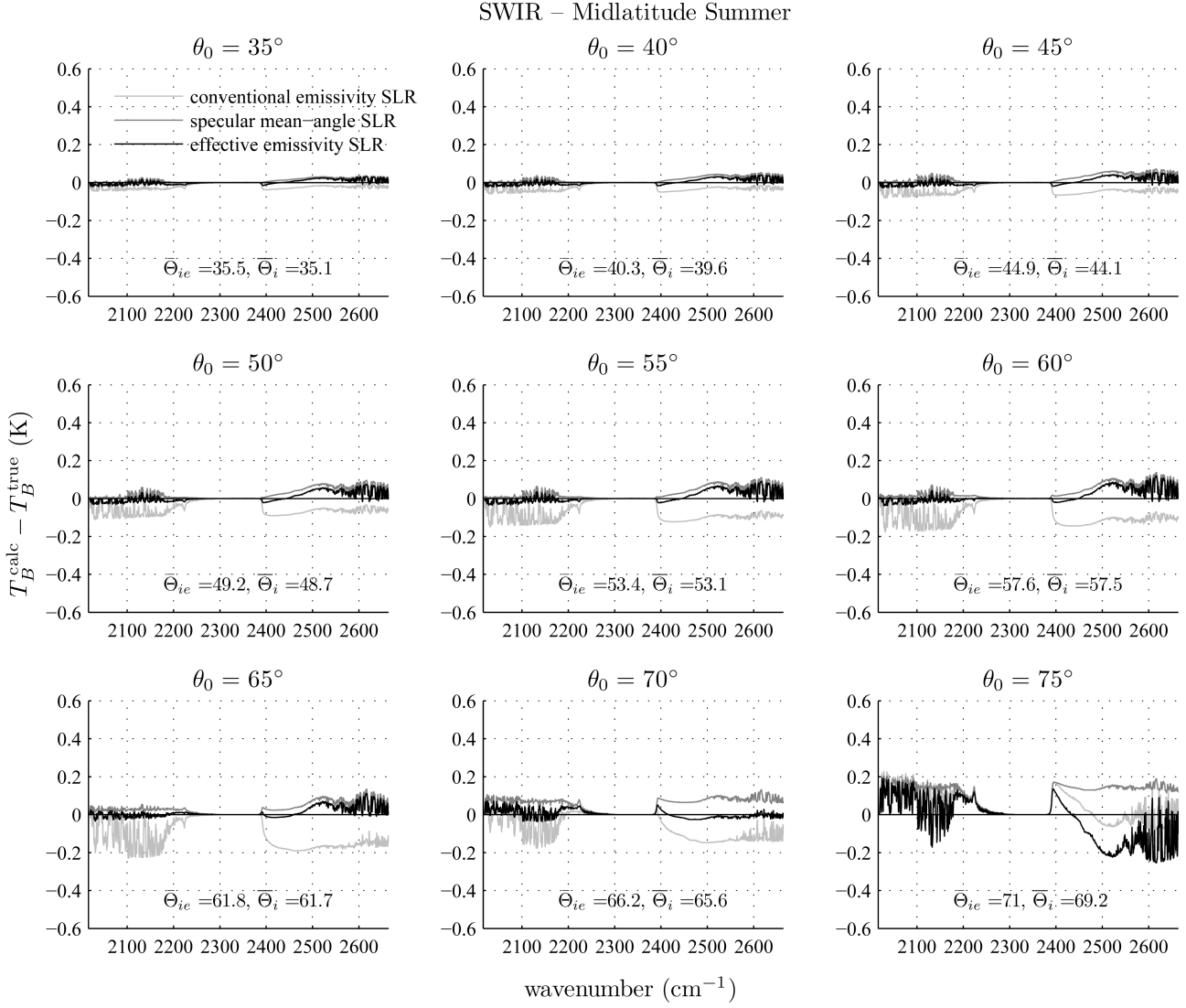


Fig. 12. Similar to Fig. 8 though for the SWIR window regions and midlatitude summer model atmosphere instead.

$\theta_0 = 65^\circ$). The conventional model also shows considerably more spectral artifacts in the residuals over $40^\circ \lesssim \theta_0 \lesssim 70^\circ$, which are correlated with atmospheric absorption features. These spectral features can be quantified in terms of spectral variability, which can reach values as high as 0.14 K (see Fig. 15, top plots).

Using the specular ensemble-mean angle approximations, Eqs. (15)–(17), the biases are reduced substantially (see Fig. 14, center plots), and spectral artifacts are far less evident (see Fig. 15, center plots), although there are some small positive LWIR biases in the more transparent atmosphere (see Fig. 10, magenta curve), with more pronounced positive biases beyond 65° (see Fig. 14, left center plot).

Finally using the effective emissivity and reflection model, Eqs. (27) and (28), spectral biases are minimized. In the LWIR windows they are reduced to within $\simeq +0.05$ K for $\theta_0 \leq 70^\circ$ and $\bar{U} \leq 12$ ms $^{-1}$

(see Figs. 14 and 15, bottom plots). A small positive bias ($\gtrsim +0.1$) appears in the LWIR at the largest angles ($\theta_0 > 72^\circ$) and wind speeds ($\bar{U}_{10} \gtrsim 8$ ms $^{-1}$). These results are reasonably consistent for the three atmospheres (see Figs. 8–13). Although residual LWIR spectral atmospheric features are very small in the tropical atmosphere (see Fig. 8 and Fig. 15, bottom left), they become somewhat more evident in the more transparent atmospheres (see Fig. 10). Even so, these do not appear to exceed the spectral random noise of current atmospheric sounders. In the SWIR windows, while some small positive biases are evident in the $2400\text{--}2700$ cm $^{-1}$ superwindow (for $55^\circ \lesssim \theta_0 \lesssim 65^\circ$, see Figs. 11–13), the total spectral biases are close to zero (see Fig. 14, bottom right), and residual spectral atmospheric features are minimal up to 70° (see Fig. 15, bottom right). We remark here that, if necessary, the small SWIR bias over $2400\text{--}2700$ cm $^{-1}$ may potentially be eliminated by

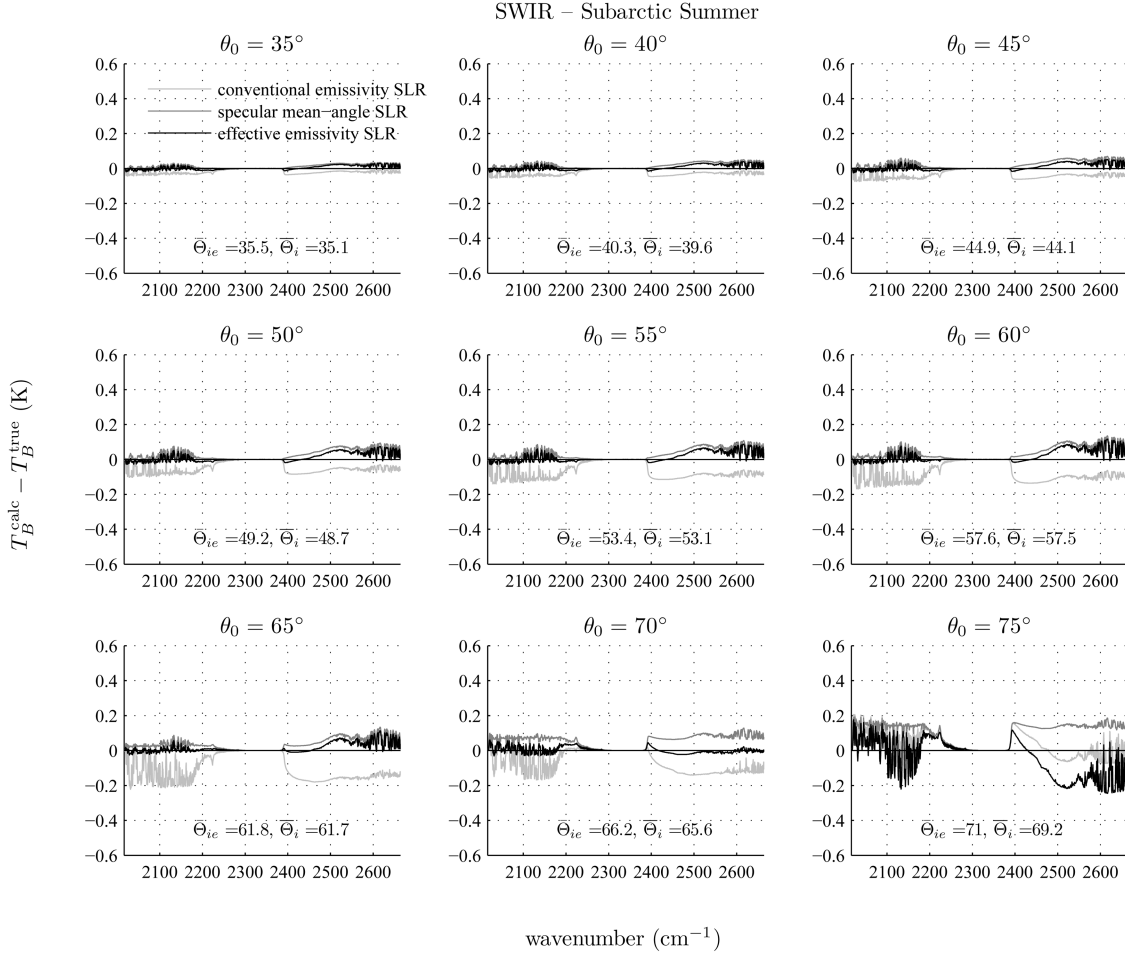


Fig. 13. Similar to Fig. 8 though for the SWIR window regions and subarctic summer model atmosphere instead.

simply conducting separate LWIR and SWIR spectral minimizations for Θ_{ie} , thus producing more than one LUT analogous to Table 3. However, we refrained from doing this in favor of model simplicity and generality.

For $\theta_0 \gtrsim 70^\circ$, it is plainly evident that all three one-stream SLR models are unreliable and yield biased results. At angles beyond 70° , an explicit case-by-case calculation of the full quasi-specular SLR given by Eq. (26) is probably necessary. The maximum observing angles of most sunsynchronous and geosynchronous environmental satellite sensors generally do not exceed 70° (excluding the extreme limbs of a geosynchronous satellite sensor scan), so the simplified model developed in this paper should thus be applicable under most circumstances.

4. Summary and Conclusions

This work has sought to develop a practical model for calculating IR ocean SLR for emission angles $\leq 70^\circ$. Because of the computational burden associated with a hemispheric double integral of downwelling column radiances, most RTMs either assume specular or Lambertian reflection, and systematic underestimation of SLR is observed for angles $40^\circ \lesssim \theta_0 \lesssim 70^\circ$

when assuming specular reflection over oceans. The dependence of bias on observing angle may have particular implications for geosynchronous satellites.

Unlike previous models that focused exclusively on emissivity, the approach presented here attempts to account consistently for both quasi-specular emissivity and reflection by introducing an effective emissivity through radiative transfer calculations. Based on simulations the model is anticipated to reduce negative bias in LWIR and SWIR microwindows by as much as 0.4 K and 0.2 K (at $\theta_0 = 65^\circ$), respectively, amounting to as much as a 0.6% correction in effective emissivity. Such a correction corresponds to a significant improvement in the context of the complete hyperspectral forward radiance model.

There are two major advantages of the model introduced in this work, namely its practicality and its testability. Because the computed effective emissivity values are valid for downwelling atmospheric radiances calculated at the observing angle, $I_{\nu a}(\theta_0)$, the model retains the same degree of simplicity as current operational algorithms based on previous methods. More importantly, however, the model calculations can be directly (and extensively) tested against radiometric observations collected from the

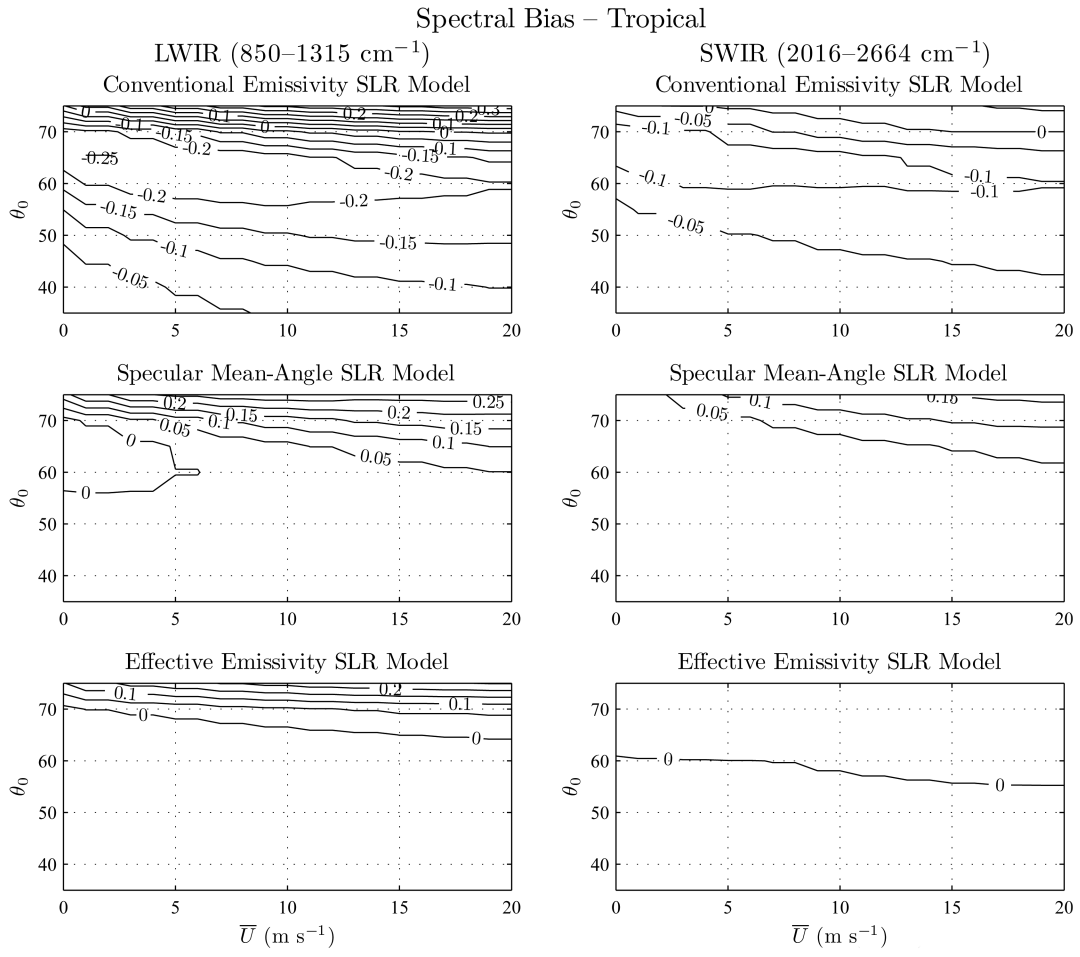


Fig. 14. Simulated SLR brightness temperature calc – true spectral bias plotted as a function of observing angle θ_0 and wind speed \bar{U}_{10} for the tropical model atmosphere. The simulation assumes the Ebuchi and Kizu [38] slope PDF and Hale and Querry [42] refractive indices. The top plots show the results using the conventional approximation, Eqs. (3) and (14), the middle plots show the results using the specular ensemble-mean angle approximation, Eqs. (15)–(17), and the bottom plots show the results using the effective emissivity and reflection model, Eqs. (27) and (28). The bias is defined as the spectral median of $T_B^{\text{calc}}(\nu) - T_B^{\text{true}}(\nu)$ in kelvin units. The left- and right-hand plots are for the LWIR and SWIR spectral bands bounded by [850, 1314.8] cm⁻¹ and [2016.3, 2663.9] cm⁻¹, respectively.

AERI-class [16] of surface-based FTS systems over the past 10 years. The datasets and results are presented in Part II. The model was designed to supersede the former Joint Center for Satellite Data Assimilation (JCSDA) emissivity model [18] within the JCSDA Community RTM.

Appendix A: Wave Slope Probability Density Function Models

We use two isotropic Gaussian wave slope PDF models: the classic model of Cox and Munk [15] and the more recent, satellite-derived model of Ebuchi and Kizu [38]. While the former model has been successfully employed in practically all previous studies requiring knowledge of mean square wave slope statistics (e.g., IR emissivity, visible ocean color, and aerosol optical depth), this work constitutes, to the best of our knowledge, the first to apply the latter model. There are a number of potential advantages to the Ebuchi–Kizu model that may render it more applicable to satellite-based remote sensing. First the authors utilized a much larger sample

(60°S–60°N, 4 yr) based on satellite data (GMS-5 visible images and NSCAT ERS-1 and 2 scatterometer data products). Then, interestingly enough, their data are shown to conform quite nicely to a Gaussian PDF, possessing little to no discernible kurtosis or asymmetry relative to wind direction (unlike Cox and Munk). This result was not considered unreasonable given that the satellite spatial resolution of their dataset was 0.25°, thus smearing the directivity of waves with respect to wind fields [38].

Both Cox–Munk and Ebuchi–Kizu provide linear parametric models of wave slope variance as a function of mean surface wind speed, \bar{U} , measured at a given height, z_s :

$$2\sigma_{CM}^2 = 0.003 + 0.00512\bar{U}(z_s), \quad z_s = 12.5 \text{ m}, \quad (\text{A1})$$

$$2\sigma_{EK}^2 = 2[0.0101 + 0.00219\bar{U}(z_s)], \quad z_s = 10.0 \text{ m}, \quad (\text{A2})$$

Spectral Variability – Tropical

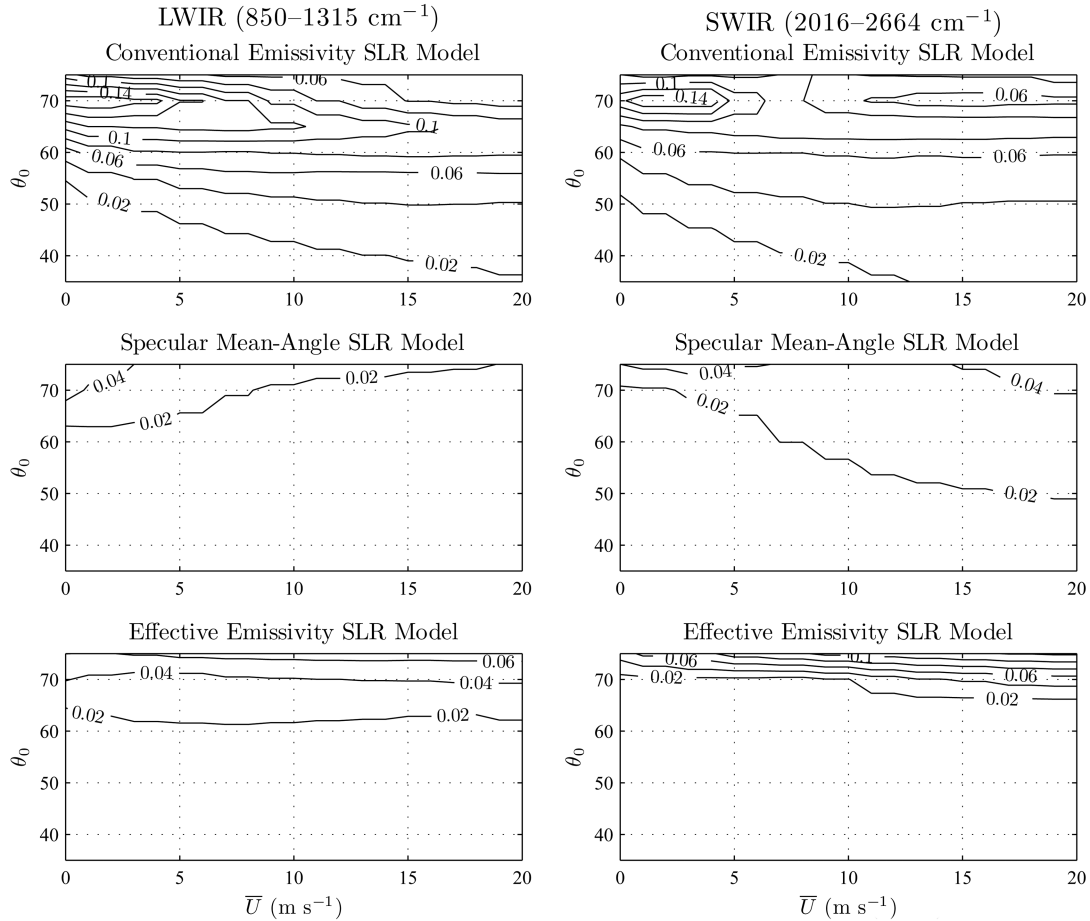


Fig. 15. Similar to Fig. 14 though showing the spectral variability defined by the robust standard deviation (i.e., the median absolute deviation divided by 0.6745) of $T_B^{\text{calc}}(\nu) - T_B^{\text{true}}(\nu)$ in kelvin units.

where subscripts CM and EK denote Cox–Munk and Ebuchi–Kizu, respectively. Note that the standard Gaussian PDF factor of 2 is consistently included in both equations; Cox and Munk [15] implicitly factored it into the left-hand side of Eq. (A1). The EK Eq. (A2) thus predicts a larger mean square slope than CM for the entire range of wind speeds (contrary to Ebuchi and Kizu's own interpretation [38]) but most notably at the lower wind speeds. The two models converge at higher wind speeds ($\bar{U} \gtrsim 15 \text{ ms}^{-1}$).

Appendix B: Surface Wind Speed Height Adjustment

The CM model Eq. (A1) is valid for wind speeds measured at a height of $z_s = 12.5 \text{ m}$, whereas the EK model is valid for the more standard mast height of 10 m . Therefore, for convenience, we normalize the CM model to an effective 10 m mast height by mapping 10 m wind speeds to 12.5 m using the method outlined below (after Smith [48] and Zeng *et al.* [49]).

The conversion of surface layer wind speeds from one height to another may be derived from the log wind profile similarity formula (assuming neutral stability) [50]:

$$\bar{U}(z) = \frac{u_*}{k} \ln\left(\frac{z}{z_0}\right), \quad (\text{B1})$$

where z is an arbitrary height, $k = 0.4$ is the von Karman constant, u_* is the friction velocity, and z_0 is the aerodynamic roughness length, which is defined as the height where $\bar{U}(z_0) = 0 \text{ ms}^{-1}$. Smith [48] obtains the following expression for z_0 over oceans:

$$z_0 = \frac{\alpha_c}{g} u_*^2 + 0.11 v u_*^{-1}, \quad (\text{B2})$$

where $\alpha_c = 0.011$ is the Charnock parameter, $v = 1.5 \times 10^{-6} \text{ m}^2 \text{s}^{-1}$ is the kinematic viscosity of air (at standard sea level pressure and temperature), and g is gravitational acceleration. Given a measured surface wind speed $\bar{U}(z_s)$ at height z_s , from Eq. (B1) the friction velocity is then given by

$$u_* = \frac{k \bar{U}(z_s)}{\ln(z_s/z_0)}. \quad (\text{B3})$$

Given Eq. (B3) we can obtain a numerical solution for the aerodynamic roughness length, z_0 , by finding the zero of Eq. (B2). Given z_0 and assuming u_* to be constant with height in the surface layer [50], $\bar{U}(z)$ can then be estimated at any arbitrary surface layer height z from Eqs. (B1) and (B3). Note that this methodology is also employed in Part II on the occasions when wind speeds were not measured at the standard 10 m height.

This work was funded by the JCSDA FY05–06 Science Development and Implementation Task (J. Yoe and J. Le Marshall). We thank C. Barnet (National Environmental Satellite, Data, and Information Service, Center for Satellite Applications and Research task monitor) and C. Dean (Perot Systems Government Services, PSGS, program manager) for their support of this project. We also extend our thanks to D. Tobin (University of Wisconsin–Madison) for providing us with AERI apodization software, E. Maddy (University of Maryland, Baltimore County and PSGS) for providing guidance on generating Fig. 1 using LaTeX, and N. Ebuchi (Hokkaido University, Japan) for correspondence pertaining to the Ebuchi and Kizu [38] paper for Appendix A. We are indebted to two anonymous reviewers who provided expert constructive feedback that we have used to improve the quality of the final paper. The views, opinions, and findings contained in this report are those of the authors and should not be construed as an official National Oceanic and Atmospheric Administration or U.S. Government position, policy, or decision.

References

1. K. Masuda, T. Takashima, and Y. Takayama, “Emissivity of pure and sea waters for the model sea surface in the infrared window regions,” *Remote Sens. Environ.* **24**, 313–329 (1988).
2. K. Yoshimori, K. Itoh, and Y. Ichioka, “Thermal radiative and reflective characteristics of a wind-roughened water surface,” *J. Opt. Soc. Am. A* **11**, 1886–1893 (1994).
3. K. Yoshimori, K. Itoh, and Y. Ichioka, “Optical characteristics of a wind-roughened water surface: a two-dimensional theory,” *Appl. Opt.* **34**, 6236–6247 (1995).
4. P. Watts, M. Allen, and T. Nightingale, “Sea surface emission and reflection for radiometric measurements made with the along-track scanning radiometer,” *J. Atmos. Ocean. Technol.* **13**, 126–141 (1996).
5. X. Wu and W. L. Smith, “Emissivity of rough sea surface for 8–13 μm: modeling and validation,” *Appl. Opt.* **36**, 1–11 (1997).
6. D. E. Freund, R. I. Joseph, D. J. Donohue, and K. T. Constantines, “Numerical computations of rough sea surface emissivity using the interaction probability density,” *J. Opt. Soc. Am. A* **14**, 1836–1849 (1997).
7. J. A. Shaw and C. Marston, “Polarized infrared emissivity for a rough water surface,” *Opt. Express* **7**, 375–380 (2000).
8. N. R. Nalli, W. L. Smith, and B. Huang, “Quasi-specular model for calculating the reflection of atmospheric emitted infrared radiation from a rough water surface,” *Appl. Opt.* **40**, 1343–1353 (2001).
9. B. G. Henderson, J. Theiler, and P. Villeneuve, “The polarized emissivity of a wind-roughened sea surface: a Monte Carlo model,” *Rem. Sens. Environ.* **88**, 453–467 (2003).
10. C. Bourlier, “Unpolarized infrared emissivity with shadow from anisotropic rough sea surfaces with non-Gaussian statistics,” *Appl. Opt.* **44**, 4335–4349 (2005).
11. C. Bourlier, “Unpolarized emissivity with shadow and multiple reflections from random rough surfaces with the geometric optics approximation: application to Gaussian sea surfaces in the infrared band,” *Appl. Opt.* **45**, 6241–6254 (2006).
12. K. Masuda, “Infrared sea surface emissivity including multiple reflection effect for isotropic Gaussian slope distribution model,” *Remote Sens. Environ.* **103**, 488–496 (2006).
13. K. Caillault, S. Fauqueux, C. Bourlier, P. Simoneau, and L. Labarre, “Multiresolution optical characteristics of rough sea surface in the infrared,” *Appl. Opt.* **46**, 5471–5481 (2007).
14. C. Cox and W. Munk, “Measurements of the roughness of the sea surface from photographs of the sun’s glitter,” *J. Opt. Soc. Am.* **44**, 838–850 (1954).
15. C. Cox and W. Munk, “Some problems in optical oceanography,” *J. Mar. Res.* **14**, 63–78 (1955).
16. W. L. Smith, R. O. Knuteson, H. E. Revercomb, W. Feltz, H. B. Howell, W. P. Menzel, N. R. Nalli, O. Brown, J. Brown, P. Minnett, and W. McKeown, “Observations of the infrared properties of the ocean: implications for the measurement of sea surface temperature via satellite remote sensing,” *Bull. Am. Meteorol. Soc.* **77**, 41–51 (1996).
17. G. L. Stephens, *Remote Sensing of the Lower Atmosphere: An Introduction* (Oxford University, 1994), p. 523.
18. P. van Delst, “JCSDA infrared sea surface emissivity model,” in *Proceedings of the 13th International TOVS Study Conference* (Sainte-Adèle, 2003).
19. M. T. Chahine, T. S. Pagano, H. H. Aumann, R. Atlas, C. Barnet, J. Blaisdell, L. Chen, M. Divakarla, E. J. Fetzer, M. Goldberg, C. Gautier, S. Granger, S. Hannon, F. W. Irion, R. Kakar, E. Kalnay, B. H. Lambrightsen, S.-Y. Lee, J. L. Marshall, W. W. McMillan, L. McMillin, E. T. Olsen, H. Revercomb, P. Rosenkranz, W. L. Smith, D. Staelin, L. L. Strow, J. Susskind, D. Tobin, W. Wolf, and L. Zhou, “AIRS: improving weather forecasting and providing new data on greenhouse gases,” *Bull. Am. Meteorol. Soc.* **87**, 911–926 (2006).
20. P. J. Minnett, R. O. Knuteson, F. A. Best, B. J. Osborne, J. A. Hanafin, and O. B. Brown, “The marine-atmospheric emitted radiance interferometer (M-AERI): a high-accuracy, sea-going infrared spectroradiometer,” *J. Atmos. Ocean. Technol.* **18**, 994–1013 (2001).
21. J. A. Hanafin and P. J. Minnett, “Measurements of the infrared emissivity of a wind-roughened sea surface,” *Appl. Opt.* **44**, 398–411 (2005).
22. M. Sidran, “Broadband reflectance and emissivity of specular and rough water surfaces,” *Appl. Opt.* **20**, 3176–3183 (1981).
23. A. M. Závody, C. T. Mutlow, and D. T. Llewellyn-Jones, “A radiative transfer model for sea surface temperature retrieval for the along-track scanning radiometer,” *J. Geophys. Res.* **100**, 937–952 (1995).
24. S. Q. Kidder and T. H. Vonder Haar, *Satellite Meteorology: An Introduction* (Academic, 1995), p. 466.
25. N. R. Nalli and W. L. Smith, “Improved remote sensing of sea surface skin temperature using a physical retrieval method,” *J. Geophys. Res.* **103**, 10527–10542 (1998).
26. X. L. Ma, Z. Wan, C. C. Moeller, W. P. Menzel, and L. E. Gumley, “Simultaneous retrieval of atmospheric profiles, land-surface temperature, and surface emissivity from moderate-resolution imaging spectroradiometer thermal infrared data: extension of a two-step physical algorithm,” *Appl. Opt.* **41**, 909–924 (2002).

27. I. J. Barton, P. J. Minnett, K. A. Maillet, C. J. Donlon, S. J. Hook, A. T. Jessup, and T. J. Nightingale, "The Miami2001 infrared radiometer calibration and intercomparison. Part II: Shipboard results," *J. Atmos. Ocean. Tech.* **21**, 268–283 (2004).
28. S. M. Newman, J. A. Smith, M. D. Glew, S. M. Rogers, and J. P. Taylor, "Temperature and salinity dependence of sea surface emissivity in the thermal infrared," *Q. J. R. Meteorol. Soc.* **131**, 2539–2557 (2005).
29. R. Niclòs, E. Valor, V. Caselles, C. Coll, and J. M. Sánchez, "In situ angular measurements of thermal infrared sea surface emissivity—validation of models," *Rem. Sens. Environ.* **94**, 83–93 (2005).
30. W. L. S. Smith, D. K. Zhou, A. M. Larar, S. A. Mango, H. B. Howell, R. O. Knuteson, H. E. Revercomb, and W. L. S. Smith, Jr., "The NPOESS airborne sounding testbed interferometer—remotely sensed surface and atmospheric conditions during CLAMS," *J. Atmos. Sci.* **62**, 1118–1134 (2005).
31. C. J. R. Sheppard, "Imaging of random surfaces and inverse scattering in the Kirchhoff approximation," *Waves Random Media* **8**, 53–66 (1998).
32. P. M. Saunders, "Shadowing on the ocean and the existence of the horizon," *J. Geophys. Res.* **72**, 4643–4649 (1967).
33. P. M. Saunders, "Radiance of sea and sky in the infrared window 800–1200 cm⁻¹," *J. Opt. Soc. Am.* **58**, 645–652 (1968).
34. C. R. Zeisse, "Radiance of the ocean horizon," *J. Opt. Soc. Am. A* **12**, 2022–2030 (1995).
35. C. R. Zeisse, C. P. McGrath, K. M. Littfin, and H. G. Hughes, "Infrared radiance of the wind-ruffled sea," *J. Opt. Soc. Am. A* **16**, 1439–1452 (1999).
36. X. Wu and W. L. Smith, "Sensitivity of sea surface temperature retrieval to sea surface emissivity," *Acta Meteorologica Sinica* **10**, 376–384 (1996).
37. N. R. Nalli, P. J. Minnett, P. van Delst, C. D. Barnet, and M. D. Goldberg, "Developments in ocean infrared emissivity/reflection modeling," in *Remote Sensing of the Ocean, Sea Ice and Large Water Regions 2005*, J. C. R. Bostater and R. Santoleri, eds., Vol. 5977 of *Proceedings of SPIE* (SPIE, 2005), p. 59770G.
38. N. Ebuchi and S. Kizu, "Probability distribution of surface wave slope derived using sun glitter images from geostationary meteorological satellite and surface vector winds from scatterometers," *J. Oceanography* **58**, 477–486 (2002).
39. C. C. Borel, "ARTEMISS—an algorithm to retrieve temperature and emissivity from hyper-spectral thermal image data," Unclassified Report LA-UR-027907 (Los Alamos National Laboratory, 2003).
40. S. A. Clough, M. J. Iacono, and J. L. Moncet, "Line-by-line calculations of atmospheric fluxes and cooling rates: application to water vapor," *J. Geophys. Res.* **97**, 15761–15785 (1992).
41. L. Pontier and C. Dechambenoit, "Determination des constantes optiques de l'eau liquide entre 1 et 40 microns. Application au calcul de son pouvoir reflecteur et de son emissivité," *Ann. Geophys.* **22**, 633–641 (1966).
42. G. M. Hale and M. R. Querry, "Optical constants of water in the 200 nm to 200 μm wavelength region," *Appl. Opt.* **12**, 555–563 (1973).
43. H. D. Downing and D. Williams, "Optical constants of water in the infrared," *J. Geophys. Res.* **80**, 1656–1661 (1975).
44. D. J. Segelstein, "The complex refractive index of water," Master's dissertation, (University of Missouri–Kansas City, 1981), p. 167.
45. D. M. Wieliczka, S. Weng, and M. R. Querry, "Wedge shaped cell for highly absorbent liquids: infrared optical constants of water," *Appl. Opt.* **28**, 1714–1719 (1989).
46. J. E. Bertie and Z. Lan, "Infrared intensities of liquids. XX. The intensity of the OH stretching band of liquid water revisited and the best current values of the optical constants of H₂O (l) at 25°C between 15,000 and 1 cm⁻¹," *Appl. Spectrosc.* **50**, 1047–1057 (1996).
47. D. Friedman, "Infrared characteristics of ocean water (1.5–15 μm)," *Appl. Opt.* **8**, 2073–2078 (1969).
48. S. D. Smith, "Coefficients for sea surface wind stress, heat flux, and wind profiles as a function of wind speed and temperature," *J. Geophys. Res.* **93**, 15467–15472 (1988).
49. X. Zeng, M. Zhao, R. E. Dickinson, and Y. He, "A multi-year hourly sea surface skin temperature data set derived from the TOGA TAO bulk temperature and wind speed over the tropical Pacific," *J. Geophys. Res.* **104**, 1525–1536 (1999).
50. R. B. Stull, *An Introduction to Boundary Layer Meteorology* (Kluwer Academic Publishers, 1988).